Università degli Studi di Padova

Department of Information Engineering

Master's Degree in Electronic Engineer

Vertical power diodes based on bulk Gallium Nitride: role of semiconductor defects

Advisor

Chiar.mo Matteo Meneghini

Università degli studi di Padova

Candidate

Martino Turrina

Academic year 2018/2019

To you, to us...

Abstract

In recent years, the significant increase in global energy demand has been driven by the significant expansion of two sectors in particular: electric mobility and renewable energy. To support this expansion, the development of more efficient and reliable power electronic devices has become essential. To date, it is estimated that only 20% of the energy produced can reach the end-user, with a large part of it lost in the various stages of conversion that make up the modern energy distribution system [1]. Within such conversion systems, the greatest loss occurs in semiconductor devices, which are a key element in reducing global energy consumption, also in response to the global warming issues we are witnessing. Most of these semiconductor devices are currently based on silicon (Si), but after the enormous improvements made through the development of manufacturing technologies and the improvement of device geometries, it is reaching its material limit. As a result, the search for new materials to further improve electronic devices has grown exponentially. This research has focused on the analysis of materials with a wide-band-gap, such as gallium nitride (GaN) or silicon carbide (SiC). These materials have already demonstrated the ability to achieve not only better performance but also higher power densities, both of which are highly requested in power applications. This revolution in the use of new materials will not only improve the performance of existing electronic devices but will also enable the development of new devices to support the applications of the future.

The objective of this thesis is to detect which are and what role defects have in semiconductors and in particular in gallium nitride devices, through the in-depth analysis of some devices based on GaN. The first section is dedicated to the analysis of the physical properties of gallium nitride and the basic information necessary to understand the design and manufacturing techniques of high-performance electronic devices. Subsequently, the various characterization techniques used to investigate the trapping phenomena are presented, in order to be able to produce devices with better performance. In the last section, the results of these characterizations on two different types of vertical GaN diodes are reported: diodes realized by polarization-doping and double-heterostructure diodes with resonant tunneling phenomena.

Sommario

Negli ultimi anni, il significativo aumento della richiesta mondiale di energia è stato trainato dalla notevole espansione di due settori in particolare: mobilità elettrica ed energie rinnovabili. Per supportare tale espansione, si è reso fondamentale lo sviluppo di dispositivi elettronici di potenza più efficienti ed affidabili. Ad oggi, si stima che solamente il 20% dell'energia prodotta riesca a raggiungere l'utente finale, con buona parte di essa persa proprio nei vari stadi di conversione che compongo il moderno sistema di distribuzione dell'energia [1]. All'interno di tali sistemi di conversione, la maggiore perdita avviene nei dispositivi a semiconduttore, che risultano essere un elemento chiave nella diminuzione del consumo di energia a livello globale, anche in risposta alle problematiche di surriscaldamento globale a cui stiamo assistendo. La maggior parte di questi dispositivi a semiconduttore è, ad oggi, basata sul silicio (Si), che però, dopo i grandissimi miglioramenti avvenuti grazie allo sviluppo delle tecnologie produttive e all'evoluzione delle geometrie dei dispositivi, sta raggiungendo il suo limite. Come conseguenza, la ricerca di nuovi materiali che permettano l'avanzamento dei dispositivi elettronici, è cresciuta in maniera esponenziale. Tale ricerca si è concentrata sull'analisi di materiali con un elevato band-gap, come il nitruro di gallio (GaN) o il carburo di silicio (SiC). Tali materiali hanno già dimostrato la possibilità di ottenere non solo migliori prestazioni ma anche densità di potenza superiori; entrambe caratteristiche molto richieste nelle applicazioni di potenza. Questa rivoluzione nell'utilizzo di nuovi materiali non soltanto permetterà di migliorare le prestazioni dei dispositivi elettronici già esistenti, ma renderà possibile lo sviluppo di nuovi dispositivi destinati a supportare le applicazioni del futuro.

L'obiettivo di questa tesi è quello di investigare quali sono e che ruolo hanno i difetti nei semiconduttori ed in particolare nel nitruro di gallio, tramite l'analisi approfondita di alcuni dispositivi basati proprio sul GaN. La prima parte sarà quindi dedicata alle proprietà fisiche di questo materiale ed alle informazioni di base necessarie alla comprensione delle tecniche di progettazione e produzione di dispositivi elettronici ad alte prestazioni. Successivamente verrano invece presentate le varie tecniche di caratterizzazione utilizzate per investigare i fenomeni di intrappolamento che prendono luogo nei dispositivi a semiconduttore, in modo da poter real-

izzare dispositivi con prestazioni sempre migliori. In conclusione verrano presentati i risultati di tali caratterizzazioni su due diverse tipologie di diodi verticali in GaN: dei diodi prodotti sfruttando il drogaggio da polarizzazione e dei diodi a doppia etero-struttura che presentano dei fenomeni di tunneling risonante.

Contents

1

Introduction

Silicon-based devices have been widely used in electronic device manufactured in the last four decades. During this period, which is indeed defined as the "Silicon Age", significant improvements have been made and so performance has reached the physical limit of this material. For this reason, there is a growing effort to find alternative materials to continue improving the sizes, functionalities, and efficiency of electronic devices.

Materials like silicon carbide (SiC) and gallium nitride (GaN), thanks to their enhanced performance, have already been used in commercially available devices for applications that demand high efficiency. In particular, has been calculated that the fundamental material base figure-of-merit (FOM) of GaN is at least five times better than SiC and nearly 1000 times better than Si. This is because the FOM is proportional to the product of carrier mobility and the critical electric field to the power of three; the latter is mostly determined by the bandgap of the

semiconductor and thus is very large in wide-bandgap semiconductors like SiC and GaN. A larger figure of merit means also increased temperature of operation, reduced dimension of the device and reduced switching, conduction, and off-state losses. In addition to the excellent figure of merit, GaN also stands out for having high operation temperature, very good thermal conductivity, large electron mobility, and saturation velocity.

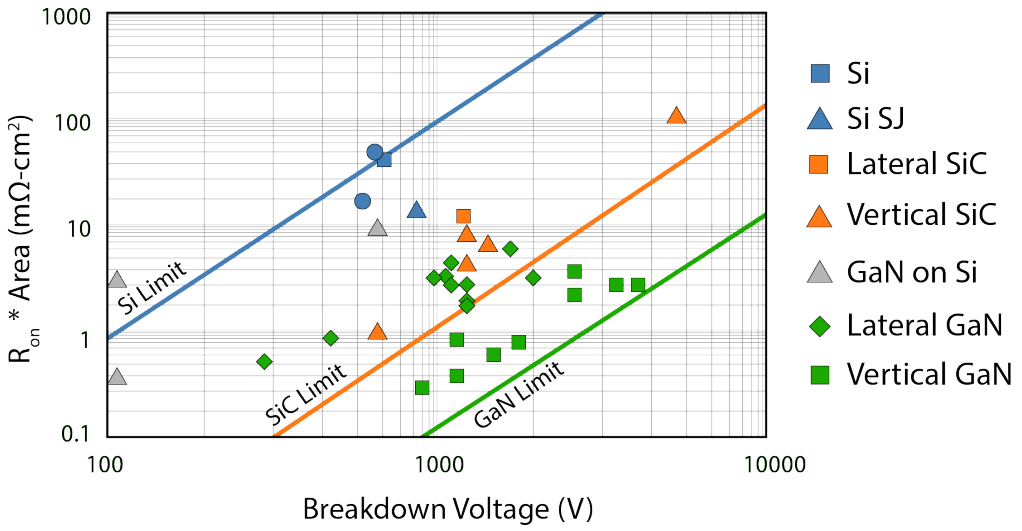

Figure 1.1: Theoretical and reported specific on-resistance vs breakdown voltage values for different semiconductors and geometries

In recent years, most efforts have focused on the development of lateral GaN devices such as HEMTs, which are fabricated inside thin layers of GaN, grown on substrates of another semiconductor. However, the high defects density and the limited breakdown voltage of these heterostructures have severely limit performance and reliability of these lateral devices.

On the other hand, using a native substrate allows the development of devices with a low concentration of defects and with totally new geometries, allowing a significant improvement in both performance and reliability. However, vertical devices manufacturing has been almost impossible until recent years, due to the very high cost of manufacturing bulk GaN substrates.

Experimental results from the analysis of these vertical devices have further demonstrated how the presence of impurities, unintentional or intentional, can have a significant effect on both the optical and electronic properties of semiconductor devices. In particular, impurity based p-type doping has proven to be inefficient in GaN and its alloys, mainly due to the high activation energy of the most commonly used acceptor dopant: magnesium (Mg). For this reason, polarization doping has been proposed to achieve highly efficient hole doping in wide-bandgap semiconductor, including gallium nitride. This technique exploits the spontaneous polarization field present in III-V nitride semiconductors and the strain-induced piezoelectric field caused by a heterojunction to create a mobile 3D electron gas which ensures high carriers density and excellent conductivity, with the use of less or even none impurity incorporation.

In recent years, there has also been a growing interest in terahertz (THz) electronic and photonic devices, thanks to the broad range of applications that terahertz waves can enable. Thanks to their excellent high electron velocity and high electron density, HEMT has been one of the first electronic device candidates for these THz applications, but it haven not yet been able to show operation at frequencies above $1\,THz$. Resonant Tunneling Diodes, instead, have been extensively studied over the last decades and recently have been used as key components in the highest frequency single-stage oscillator to date [2]. III-Nitride based RTDs however, have only recently showed repeatable room temperature resonant tunneling transport and eventually THz oscillation. This was due to the aforementioned lack of low defects density substrates which was especially a problem for GaN.

For these reasons, an in-depth analysis of how defects impact the performance of vertical GaN-based devices is mandatory to achieve the specifications required by the electronics and photonics applications of the future.

2

Gallium Nitride

Gallium nitride (GaN) is a binary III-V compound which means it consists of an atom of the third group of the periodic table, gallium, and an atom from the fifth group, nitrogen.

Gallium nitride and the others III-V compounds, in particular the nitrides, have interesting physical and chemical properties that make them suitable for the manufacturing of high power and radio frequencies devices, in which such high performance are not achievable by silicon-based ones. Of all these III-V semiconductors compounds, the gallium nitride and the various alloys based on it (like the AlGaN) have superior properties and have therefore allowed the development of a series of new high performance devices capable of supporting the technologies of the coming years. In particular GaN not only has a big direct band-gap of 3.4 eV (which allows its use also in optoelectronics devices), but has excellent electron transport properties, high breakdown voltage and high thermal conductivity [3].

Figure 2.1 compares some important parameters for semiconductor devices based on different materials; as can be noticed, GaN-based devices have better performance in every aspect, if compared to silicon or gallium arsenide based devices.

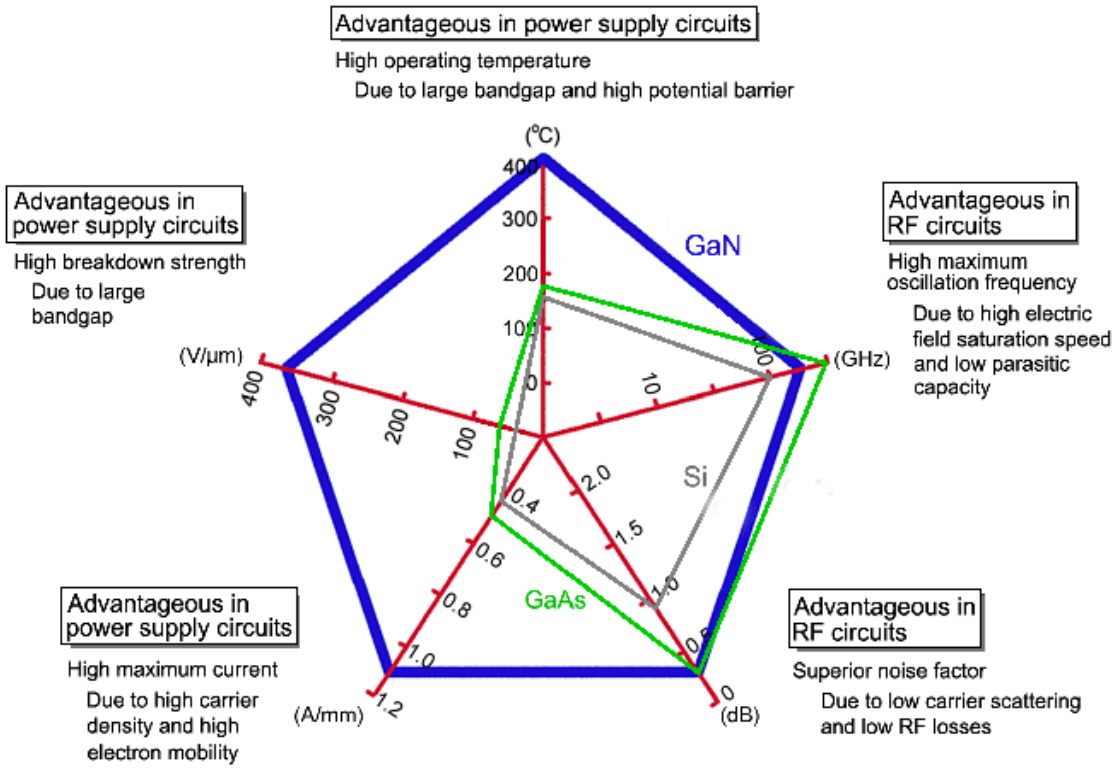

Figure 2.1: Performance comparison between Silicon, Gallium-Arsenide and Gallium Nitride

For these reasons, gallium nitride has become one of the candidate material for the realization of high power electronic and optoelectronic devices.

Despite that GaN has been studied more extensively than all the other III-N semiconductors, further exploration is still needed to match the knowledge that we have for material such as silicon or gallium arsenide.

2.1 Crystal structure and electrical properties

To better understand how a GaN-based device works, it is necessary to study the structure and the properties of the lattice formed by gallium and nitrogen.

These two elements can merge into two main crystal structures: zinc blende (ZB) and wurtzite (WZ). Only the second one is a thermodynamically stable structure and so it is the most important. The wurtzite type materials have a wider bang-gap as the lattice became more compact (see Figure 2.2) and, in the case of GaN, the structure consists of a hexagonal unit cell with an ionic bond between gallium and nitrogen due to the large difference in electronegativity of the two atoms.

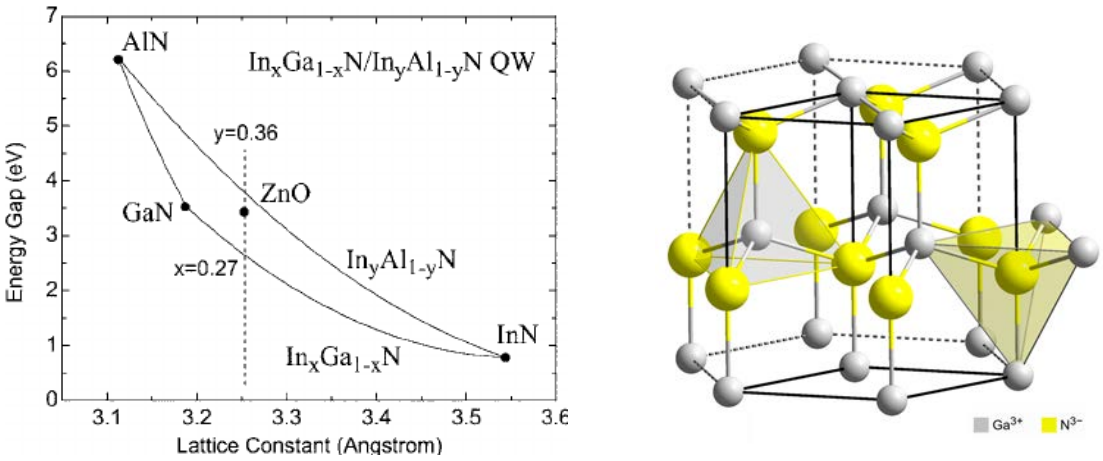

Figure 2.2: Relation of the lattice constant compared with the energy gap in different materials and a representation of the lattice structure of GaN

The hexagonal structure of GaN present a spontaneous polarization charge along the vertical c-axis, which is one of the causes of the particular electronic properties of this material. This is caused by the fact that nitrogen has a much higher electronegativity with respect to gallium and so they will have cationic (-) and anionic (+) characteristics respectively and so the resulting molecule is a dipole.

Furthermore, if gallium nitride is grown on or close to other materials with a different lattice constant it can lead to the creation of a piezoelectric polarization charge which adds to the

spontaneous one. In these conditions, free carriers are created at the hetero-interface to neutralize the fixed spontaneous and piezoelectric polarizations. The resulting polarization, which is more than ten time higher in wurtzite GaN than in other III-V or II-VI semiconductors compound, and the resulting electric field can produce high densities of interface charge enabling the realization of devices without the use of intetional doping.

To create more differentiated materials, it is also possible to merge different semiconductors, based on the same material, to obtain a new alloy that acquires the characteristics of the initials semiconductors in proportion to the concentrations following the Vegard law. For example, the aluminum gallium nitride ($Al_xGa_{1-x}N$) composed of a x fraction of AlN and a (1-x) fraction of GaN will have an expected band-gap which can be calculated as follows:

$$E_{g\,AlGaN} = xE_{g\,AlN} + (1-x)E_{g\,GaN} \tag{2.1}$$

2.2 Fabrication Tecniques

In order to obtain high-performance and reliable devices, expensive and complex fabrication processes are required. In fact, to achieve excellent performance, it is mandatory to start from a perfect crystal material with the lowest possible density of dislocations, defects or contaminants.

To fabricate devices based on gallium nitride we basically have two options:

- fabricate a bulk GaN substrate and then grow our devices on top of it;
- start from a foreign substrate with possibly a similar reticular constant and thermal expansion coefficient and grow GaN devices over it.

In the first case, we obtain a homo-epitaxial structure, typically resulting in high-quality devices. The downside of fabricating GaN-on-GaN devices is that the process is difficult and expensive

also because the fabrication of big GaN wafer (8 or 12 inches) has not yet been achieved. For these reasons, bulk GaN device manufacturing remained almost impossible until recent years.

Multiples techniques for the growth of bulk GaN substrates have been reported in literature and here we will present some of them [4]:

- HPSG (High-Pressure Solution Growth): this is the most mature process for substate growth of most semiconductors but in the case of gallium nitride the higher melting temperature and the high equilibrium pressure of N_2 makes GaN growth very difficult. Due to the low solubility of nitrogen in Ga, the growth rate is very limited and so resulting crystals are very small. However, HPSG has been the technique able to produce the highest quality GaN crystals with very low dislocation densities;

- LPSG (Low-Pressure Solution Growth): this is a variation of the HPSG technique in which liquid sodium with low content of gallium is used instead of a nitrogen solution. The results obtained by this method are quite similar to the one obtained by HPSG but with lower temperature and pressure conditions (temperature near 850°C instead of 1600°C);

- Ammonthermal growth: in this technique polycrystalline GaN is dissolved in ammonia under high temperature and high pressure conditions. Exploiting some solubilizing agent or mineralizer, gallium nitride is grown. This process brings a low growth rate and high-quality material production but benefits from reasonable temperature and pressure conditions;

- Hydride Vapor Phase Deposition (HVPE): this technique consists of two main reactions: the first for forming chloride gas of group III metal at low temperature and the second is the reaction between chloride metal and ammonia to form the nitride layer at higher temperatures. This is considered the best method to obtain thick GaN layers without

prohibitive growth conditions. A scheme of the operation of HVPE can be seen in Figure 2.3.

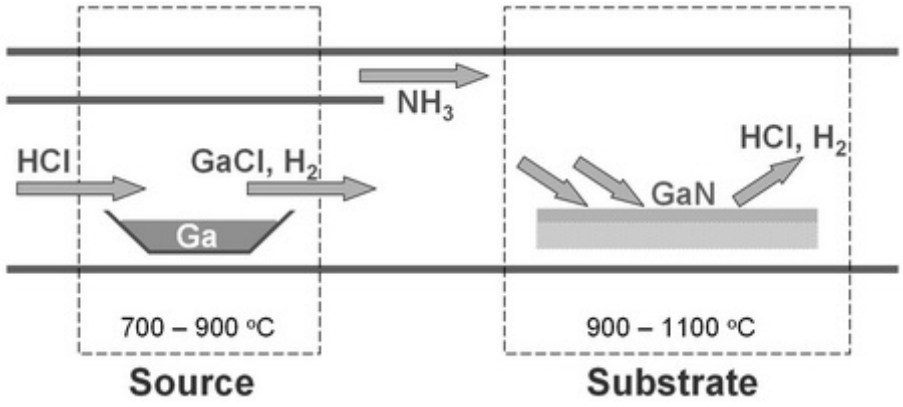

Figure 2.3: Schematic diagram of Hydride Vapor Phase Deposition (HVPE)

The ongoing research to improve these technologies is however bringing significant results; with current techniques, it has been shown that 4-inch diameter GaN substrates can be made in reasonable times with low defect densities.

In the case of a hetero-epitaxy instead, the techniques are easier and cheaper but they may produce lower quality devices due to the high defect density. In particular, to ensure a low density of dislocation, it is crucial to reduce the mismatch between the two materials.

The most used substrates for GaN growth are:

- Sapphire (Al_20_3): despite the not optimal reticular match, it was one of the first substrates used in the growth of GaN thanks to its low cost of production. The mismatch is usually alleviated by introducing a nucleation layer (mainly AlN) between the substrate and the GaN buffer;
- Silicon Carbide (SiC): it has better reticular coherence with GaN than sapphire and a remarkable thermal conductivity which allows improving the performance of the resulting devices. The problems with these type of substrate are the high production cost (even if

it is lower than growing GaN substrate) and the high difficulty in obtaining substrates with an acceptable density of defects;

- Silicon (Si): it is probably the easiest and cheaper material to grow, so it is used a lot as a substrate for gallium nitride. Additionally, since it is possible to exploit processes and machinery that are already used for standard Silicon devices, the production of big GaN-on-Silicon wafers (8 or 12 inches) is very easily and cheaply achieved. However, GaN and Si have a large lattice mismatch that recently has been overcome thanks to the development of sophisticated growth techniques, significantly lowering the density of defects (under $10^8\ cm^{-2}$).

In Figure 2.4 a comparison between different substrate and their parameters is reported.

	Sapphire	SiC	Si	GaN
Lattice mismatch (%)	16	3.1	−17	0
Linear thermal expansion coefficient ($\times 10^{-6}$ K^{-1})	7.5	4.4	2.6	5.6
Thermal conductivity (W cm^{-1} K^{-1})	0.25	4.9	1.6	2.3
Cost	Cheap	Expensive	Cheap	Very expensive
Dislocation density of GaN films grown on substrate (optimized) (cm^{-2})	Low 10^8	Low 10^8	Low 10^8	10^4–10^6

Figure 2.4: Properties of different candidate substrates for GaN epitaxy and the possible dislocation density obtainable

Once the substrate is created (whether it is of GaN or of other materials), various semiconductor layers are deposited over it in order to obtain the desired structure.

The most common techniques for the production of Gallium Nitride and other semiconductor devices are:

- MBE (Molecular Beam Epitaxy): this technique is based on the creation of a high vacuum atmosphere in order to avoid collision between atoms or particles involved in the

process. The most important aspect of MBE is the very high deposition rate of around 3000 nm/h that allows the growth of very precise and thin layers. With this technique, it is possible to control the growth thickness up to a single atomic layer. The absence of carrier gases and the high-vacuum environment results in the highest achievable quality and purity for semiconductor growth. In fact, this technique is used for the production of highly reliable and performing devices, at the expense of the higher cost of production. A schematic diagram of MBE can be see in Figure 2.5;

- MOCVD (Metal-Organic Chemical Vapor Deposition): in this technique, finely dosed ultra-pure gases are heated before being injected into a reactor, in which a semiconductor wafer is positioned on a rotationally base (see Figure 2.5). Surface reactions of the gases containing the required chemical elements create the conditions for epitaxial growth of the desired semiconductor. The fact that this process is performed at atmospheric pressure, makes it very cheap and scalable. The most used precursors are $Ga(CH_3)_3$ for gallium, $Al(CH_3)_3$ for aluminum whereas nitrogen is obtained from ammonia (NH_3).

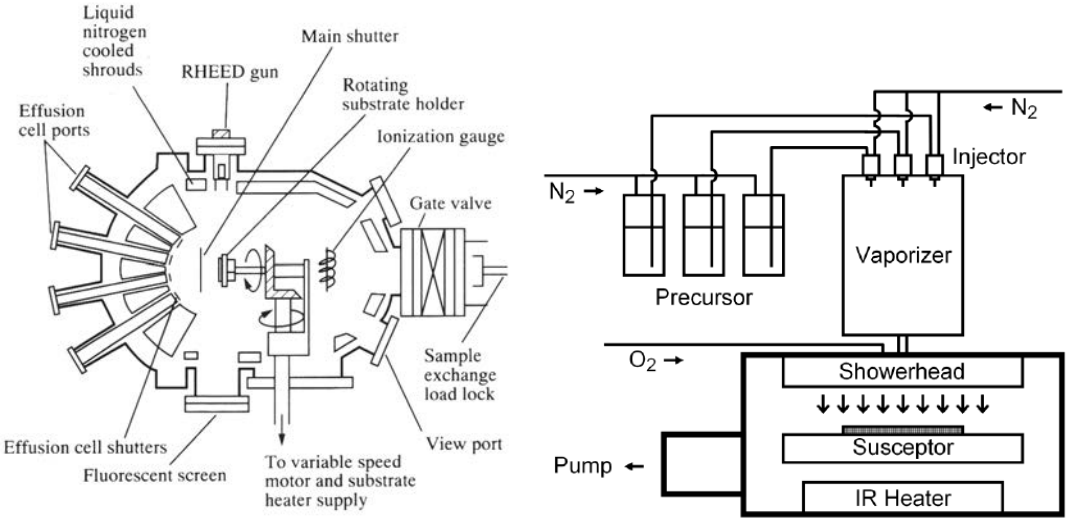

Figure 2.5: Schematic diagram of Molecular Beam Epitaxy (on the left) and Metal-Organic Chemical Vapor Deposition (on the right)

2.3 N- AND P-TYPE DOPING

To fabricate various GaN-based devices it is essential to be able to perform both n- and p-type doping.

In the case of GaN, n-type doping is quite straightforward and can be achieved by adding, for example, silicon or germanium to the material. On the other side, p-type is quite problematic, mainly because the most used impurity that can produce p-type GaN, magnesium (Mg), suffers from a lot of limitations. In particular, it has higher ionization energy than typical acceptors (in GaN this energy can be as high as $250\ meV$) and so high concentrations of Mg (even 100 times higher than normal) are required to achieve the desired hole concentration. This increase in the use of dopants will strongly affect the electron and hole mobilities and so the efficiency of the resulting devices. In addition, it is known that Mg-doped GaN needs to be subjected to treatments such thermal annealing or electron-beam irradiation in order to activate the acceptors [5].

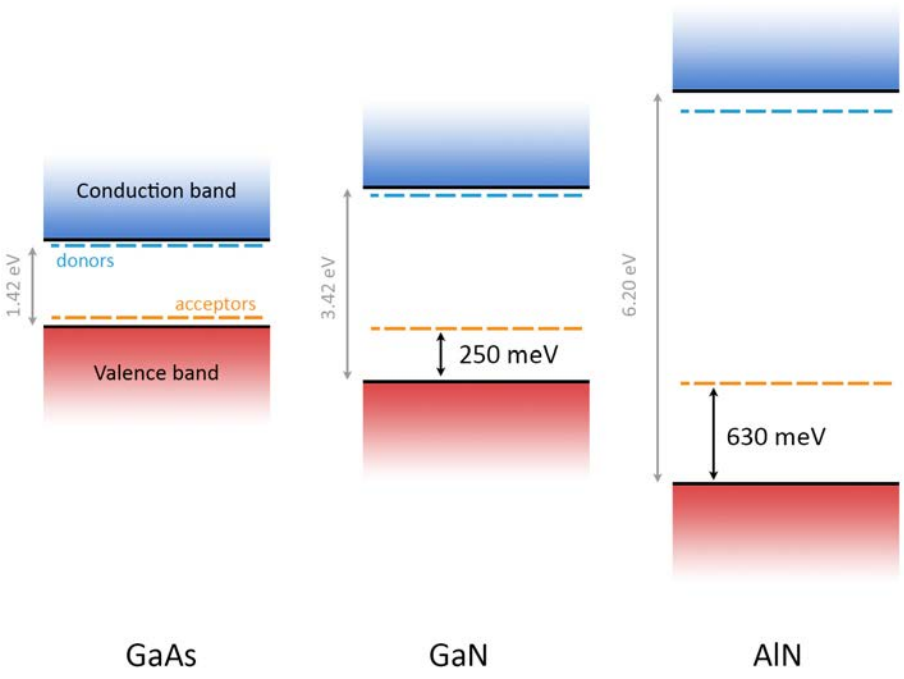

Figure 2.6: Ionization energy of Magnesium in different semiconductors

In order to overcome the limitations of magnesium and obtain efficient doping in III-nitrides, beryllium (Be) was used. Unfortunately, the Be atoms tend to occupy interstitial positions and therefore act as double donors. The result is that the material doped with beryllium is semi-insulating if heavily doped and so these element was abandoned as p-type dopant in wide band-gap nitrides [6].

In addition, in materials with an even higher band-gap than GaN, such as AlN which has a band-gap of 6.2 eV, it is even harder to obtain high doping efficiency at room temperature both using Be or Mg, due to the link between ionization energy and bandgap (seen Figure 2.6).

To avoid this problem, it is possible to achieve efficient p-type doping and hole injection in wide-band-gap semiconductors exploiting the phenomenon called polarization doping. The spontaneous polarization due to the ionic component in GaN bonds and the piezoelectric polarization due to the strain induced by the formation of a heterostructure can lead to the formation of high sheets of free charge at the hetero-interface. This charge generates a high electric field and a bending of the energy-bands such that a two-dimensional electron gas (2DEG) is formed, without the need for impurity doping. Such two-dimensional electron gas is the key to the functioning of nitride high-electron-mobility transistor (HEMT), that have shown superior performance than transistor made from any other semiconductor [7].

It is also possible to obtain three-dimensional electron gases (3DEG) through the use of GaN alloys with gradual variation of the concentration, for example of aluminum in AlGaN, so as to distribute the effect of the polarization field along the third dimension as well. This doping technique is achievable both with help of impurity dopant and also without it. We will further analyze this particular method of doping in chapter 4, which is entirely dedicated to polarization-doped diodes.

2.4 Vertical devices

Even if lateral devices, such as HEMT, have been the most studied GaN-based layouts for years, thanks to the improvements in production of moderate sized bulk GaN substrates, vertical devices have recently gained interest. Lateral devices suffer from several disadvantages that have limited their success; in particular, they typically have low breakdown voltage and high defect density.

The big advantage in breakdown voltage of these vertical devices is because the high electric field is held by the bulk of the material, rather than by the surface. This brings to devices capable to stand higher electric fields with much lower total device area, since the active region develops also in the vertical direction. Under optimal conditions, breakdown voltage as high as 3.7 kV has been achieved in a p-n diode with a $40\ mum$ thick drift layer [8].

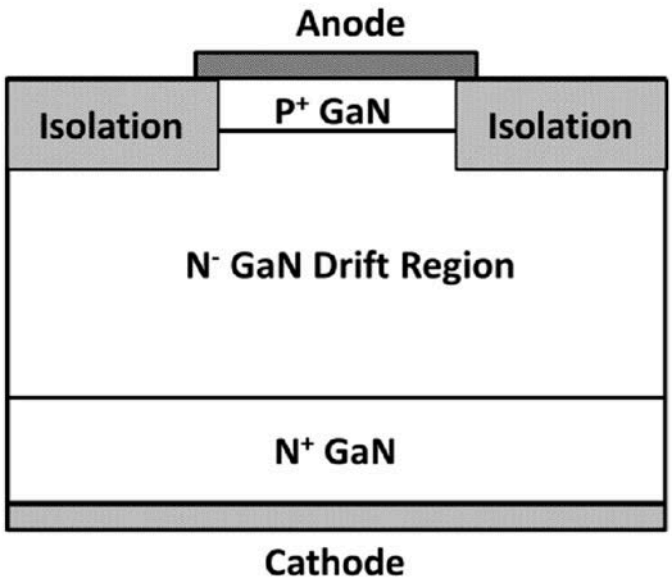

Figure 2.7: Schematic view of a vertical GaN p-n diode on bulk Gallium Nitride)

Another big advantage of these devices is the low dislocation density in the film grown over bulk GaN of 10^4 to $10^7\ cm^{-2}$, or at least two order of magnitude lower than GaN films grown on

sapphire, silicon or SiC substrates [9]. Also, the lack of a buffer layer, mandatory in lateral devices to ensure low dislocation densities in presence of low lattice match, can lead to less charge trapping phenomena and so an improvement in the reliability of the devices.

All these shortcomings for existing lateral devices coupled with the benefits of the vertical ones, provide strong motivation for the development of vertical power devices.

2.5 Defects

To optimize growth techniques and therefore improve performance of GaN devices, it is important to identify and localize traps inside the epitaxial structure. These devices can present different type of defects (also visible in Figure 2.8):

- Native defects: they are due to the crystal structure of gallium nitride and are mainly present in the bulk. They can be divided in: vacancies if there is missing gallium or nitrogen atoms in their usual position in the lattice, anti-sites if, for example, a nitrogen atom takes the position in the lattice of a gallium atom or vice versa, and interstitials if an atom of nitrogen or gallium is present where no element should be present;

- Impurities: they are atoms of other elements inside of the GaN lattice. They can be dopant atoms (magnesium, silicon, iron or carbon) or impurities coming from the atmosphere in which the device were growth (oxygen or hydrogen). These impurities can be interstitial if they are located where typically no element should be, or substitutional if they have taken the place of a Ga or N atom in the lattice. These foreign elements cause the creation of allowed states inside the energy gap;

- Extended defects: they are created by more than one atom misaligned resulting in a large defect. They can be two- or three-dimensional propagation of native defects or they can be originated from particular positioning of the crystalline lattice (e.g. stacking fault).

- Surface defects: they can be single or extended defects located at the last layer of the material. The fact that at the interface the crystal structure change abruptly can lead to the formation of dangling bonds, bonds with impurities and loop bonds. However, the concentration of these surface defects can be alleviated through some passivation techniques.

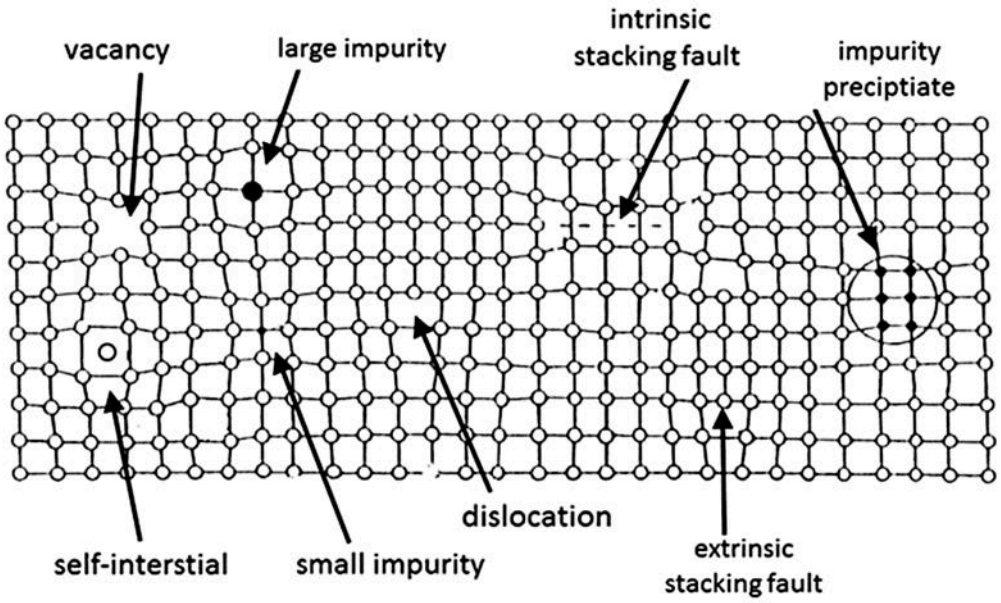

Figure 2.8: Visual representation of different type of defects that can be found in semiconductors

However, in vertical devices based on bulk GaN, the most frequent defects are the native ones, which are present in low densities thanks to the advanced growth fabrication techniques.

One of the most common impurities in GaN and in other III-nitrates, is carbon. This element is often unintentionally incorporated during growth or it is deliberately introduced as a dopant to produce p-type or semi-insulating GaN for use in HEMTs or in similar devices [10]. Despite its strong presence, the properties of carbon impurities are not fully clear. Early studies have assumed that carbon acts as an acceptor when substituting on the nitrate site (C_N) and as a donor in the cation site [11]. However, more recent analysis, based on hybrid functional calculation, has shown that C_N is the most common configuration of carbon impurities in n-type GaN or

in AlN and that it is not a shallow acceptor but instead a very deep one with ionization energy of 0.8-0.9 eV [12]. The recalculated configuration coordinates diagram, reported in Figure 2.9, shows how the transition from C_N^0 to C_N^- lead to an emission process with a energy of around 2.14 eV corresponding to an emission in the yellow region of the spectrum and how the transition from C_N^+ to C_N^0 lead to an emission process with a energy of around 2.7 eV corresponding to an emission in the blu range of the spectrum. This result demonstrates that carbon impurities in GaN can lead to both yellow and blue emission depending on the position of the Fermi level in the sample [13]. It is also important to note that carbon is not the only source of these photoluminescence phenomena in GaN but it is certainly one of the most interesting given its great presence in modern substrates and the little knowledge we have about it.

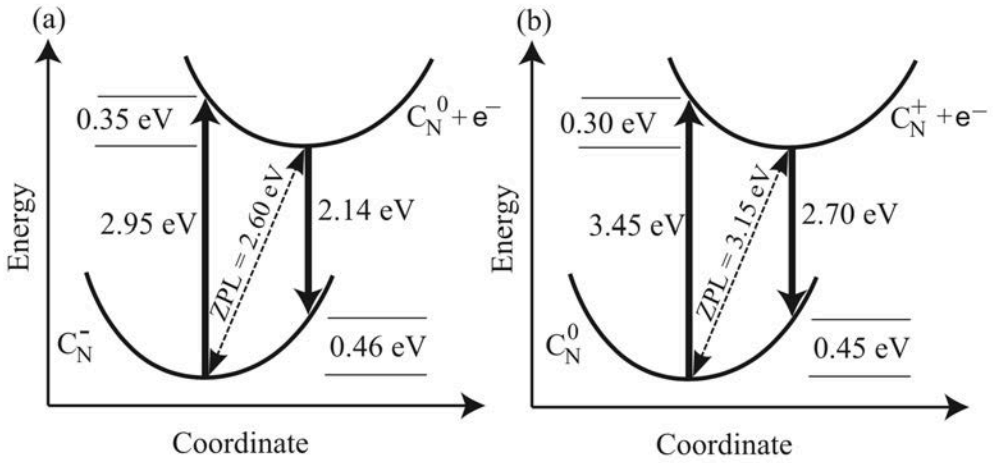

Figure 2.9: Configuration-coordinate diagram for the C_N impurity in gallium nitride

2.6 Deep-level traps

If the energy required to remove an electron or hole from a traps is much larger than the characteristic thermal energy kT, the trap will be referenced as deep-level. These defects can interfere with some types of doping by compensating the dominant charge carrier type or can offer intermediate state inside the band-gap so lowering the total efficiency of the device.

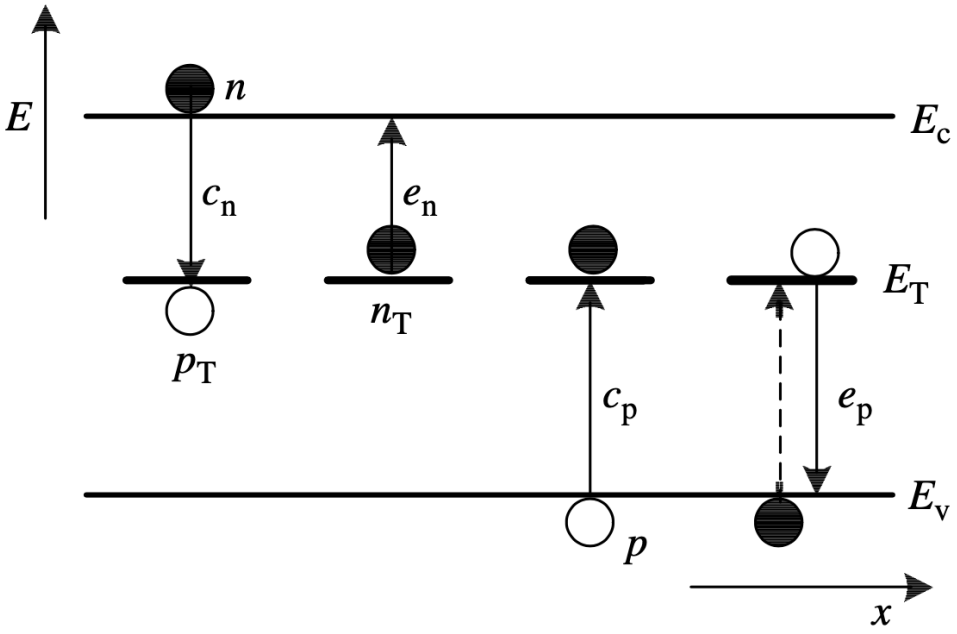

Figure 2.10: Band diagram of a semiconductor with deep-level impurities

Deep levels can capture and afterward emit a carrier which can be both an electron or a hole. The probability of emission, described by the emission coefficient, strongly depends on the position of such level with respect to the conduction and valence bands. Traps can be classified as donors or acceptors; donors if they donate, for example, an electron to the conduction band, or acceptors if they accept an electron from the valence band.

Defects can be identified by their charge state, ionization energy and capture cross section. In particular, knowing that the ionization energy of a localized level inside the band-gap E_T is related to the thermally activated ionization rate rate e, it is possible to extract this parameter by an Arrhenius plot, by analyzing the dependence of this rate to the temperature.

In presence of a strong electric field, the rate of charge emission from traps can increase substantially due to potential band lowering, direct and photon-assisted tunneling. In particular, if we consider a trapping center in presence of a strong electric field, the barrier will be lowered in the direction of the field. This condition implies that the electron is required less energy in order

to escape from the trap. This field-assisted emission mechanism is known as the Poole-Frenkel effect [14].

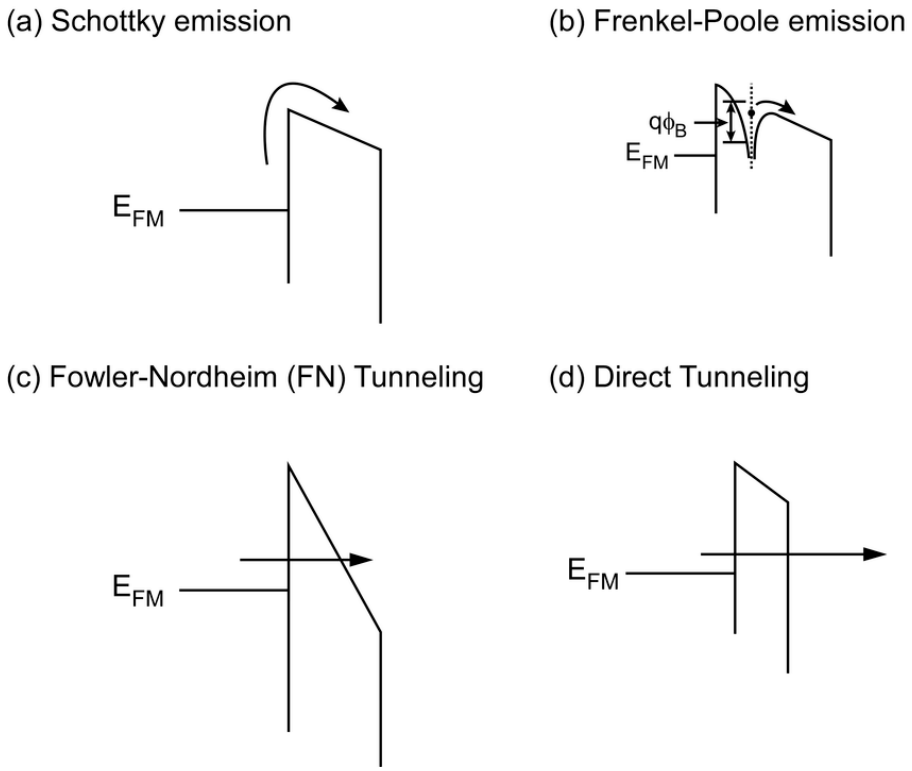

Figure 2.11: Schematic representation of different emission mechanisms for a trapped electron including the Poole-Frenkel effect

3

Characterization techniques

In order to fully characterize the chosen devices, we carried out electrical and optical characterizations.

To perform these characterizations, the wafers are positioned on a plate called chuck which is mounted inside of a probe station. This platform often contains a convenient vacuum system to ensure the stability of the wafer in question and a temperature conditioning system useful for taking measurements at different ambient temperatures. The chuck is often positioned inside a closed structure which provides mechanical support to all the equipment necessary to contact the devices and also acts as a Faraday cage to protect the devices from incoming external electromagnetic interference (including also incident outside light). Next to the chuck, there are micro-manipulators on which different types of tips are mounted depending on the measurement to be made and the size of the device. A set of knobs makes it possible to move the

wafer on all the axes and also to move the tips to reach any device on the wafer. These tips are then connected to the necessary instruments via BNC, triaxial or high voltage cables and these instruments are usually controlled via the GPIB interface and a PC running a LabView program specifically designed for that specific measurement. To facilitate the contact of the devices, a microscope is positioned above the chuck and, in some cases, it includes also a camera which permits the acquisition of photos or emission measurements of the wafer.

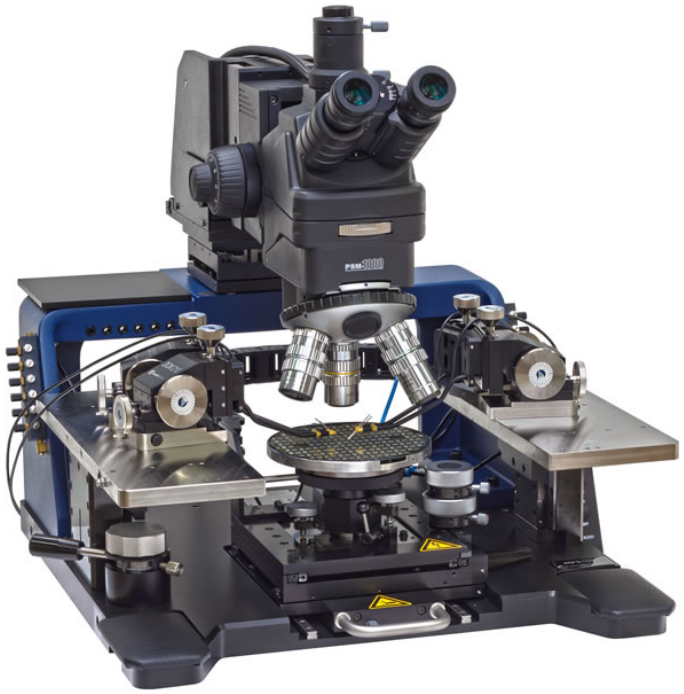

Figure 3.1: Image of a probe station with microscope, manipulators and, in the middle, the chuck holding the wafer in position

3.1 Preliminary electrical characterization

Before entering into advanced measurements capable of characterizing the trapping mechanisms that affect the performance of the devices, it is necessary to characterize its DC behavior. In particular current-voltage measurements are essential because they allow obtaining the fundamental parameters of the devices, such as series resistance and threshold voltage.

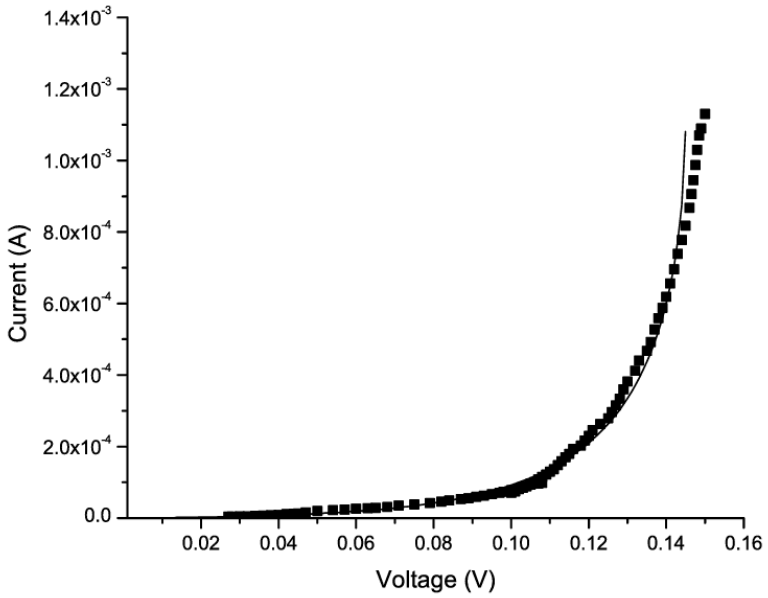

Figure 3.2: Example of a IV measurement of a diode

These current-voltage measurements are often repeated under different conditions to see the response of the device to these changes: in particular temperature and light are often used to study changes in the device behavior at high or low temperatures or under light of different wavelengths.

3.2 Cryogenic probe station

In order to perform measurements at extremely low temperature, it is necessary to use a cryogenic probe station which exploits the flow of liquid hydrogen or liquid helium to reach temperatures below $10\ K$. With a special stage, it is possible to reach even very high temperatures to obtain measurements in a large temperature range without changing probe station or instruments.

The probe consists of multiple layers of protection starting from an external vacuum chamber, an intermediate radiation shield and a final stage on which the wafer will be positioned. The temperature of all these elements is monitored during use to avoid going over the limit temper-

ature of every component of the probe. The temperature is therefore regulated through the use of a specific controller which can monitor and adjust the temperature of the various stages. To avoid condensation and minimize heat transfer, the chamber in which the device is located is under high-vacuum conditions, thanks to the presence of a high-vacuum pump.

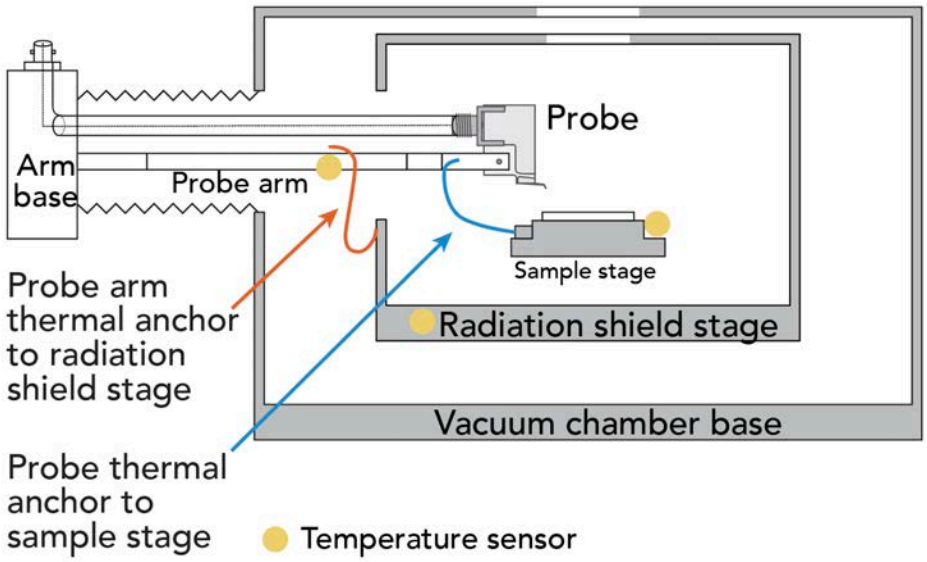

Figure 3.3: Schematic view of the cryogenic probe station structure

It is possible to contact the wafer through the use of isolated arms which are mounted on micro-manipulator mechanisms. On these arms, compensation must be made in order to offset any arm movement during variable temperature experiments. Without a compensating probe, significant ramping of sample stage temperatures may result in contact quality changes during measurements, possibly shifting the tip enough to leave its contact pad. Furthermore, to avoid injecting unwanted heat into the sample device via the probe arms, the arms and probes must be thermally anchored to other sections of the probe.

To carry out optical measurements it is also possible to use a specific arm equipped with a mounting mechanism for an optical fiber which will be positioned over the device under analysis and then connected to, for example, a Compact Array Spectrometer (CAS). Above the probe

Figure 3.4: Image of a cryogenic probe station with a central chamber for the device, six arms and a light on top

station, there is a lamp that illuminates the sample through a window and a camera that allows to photograph or view the sample. The entire structure is mounted on a pneumatic base which helps in eliminating every vibration which could ruin or alter the measurements.

3.3 Deep Level characterization

In order to characterize defects in semiconductors, we need some advanced experimental techniques such as Capacitance Deep-Level Transient Spectroscopy (C-DLTS) or Deep-Level Optical Spectroscopy (DLOS). These techniques allow us to measure the concentration of the defects and to extract their signatures like activation energy and capture cross-section. These parameters are very useful because semiconductor devices performance are strongly influenced by defects, so their characterization is very useful to engineer new more reliable and performing devices.

3.3.1 Capacitance-Deep Level Transient Spectroscopy (C-DLTS)

The Capacitance Deep Level Transient Spectroscopy technique is based on the analysis of the variation of the capacitance of a pn junction under reverse bias in the presence of trapping states. In particular, during a constant reverse bias condition, a space-charge-region (SCR) is created and its capacitance will depend on its width. If the concentration of electrons trapped into the deep levels changes, the SCR will change its width to compensate and so leading to a variation in the measured capacitance. Analyzing the resulting capacitance transient it is possible to obtain information regarding the deep levels present in the device. For example, if the capacitance variation is positive we are dealing with majority carrier traps and, in the opposite case of a negative variation, we have minority carrier traps.

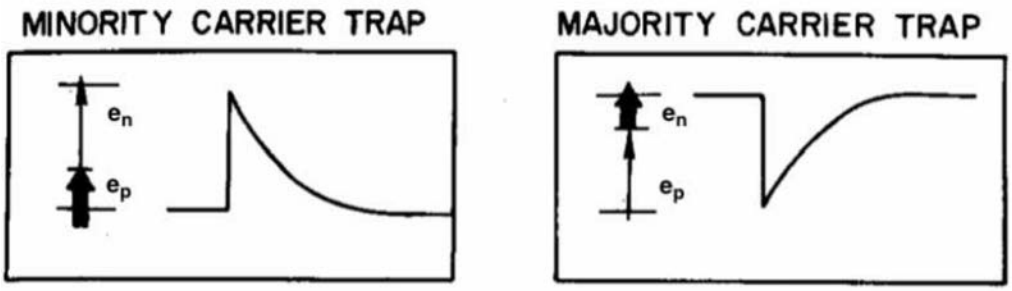

Figure 3.5: Capacitance transient in a pn junction induced by a minority (sx) or majority (dx) carrier trap

It is also possible to estimate the density of defects analyzing the capacitance transient. In particular, assuming that the initial density of traps occupied by an electron $n_T(0) = N_T$ and the same density at regimie $n_T(\infty) = 0$ we can write

$$\frac{C_\infty - C(0)}{C_\infty} = \frac{n_T(0) - n_T(\infty)}{2N_D} = \frac{N_T}{2N_D} = \frac{\Delta C}{C} \tag{3.1}$$

were C_∞ is the steady-state capacitance value, $C(0)$ is the initial capacitance value, and N_D is the n-type dopant concentration. The defect concentration can therefore be written as:

$$N_T \approx 2\frac{\Delta C}{C} N_D \tag{3.2}$$

To accomplish the previously assumed condition of $n_T(0)$, it is necessary to apply a filling voltage: in this condition traps can capture carriers and thus approach the condition of total filling. Typically the filling voltage is in module lower than the reverse bias voltage that will be applied later during the measurement.

C-DLTS measurements can be repeated at various temperatures and at different reverse voltages in order to analyze different deep levels. The variation of the temperature results in a change of the time constant of the capacitance transient and so can give us information about the emission time constant. These time constant can be plotted for every temperature to obtain an Arrhenius plot from which we can extract the activation energy and the cross section of the deep levels.

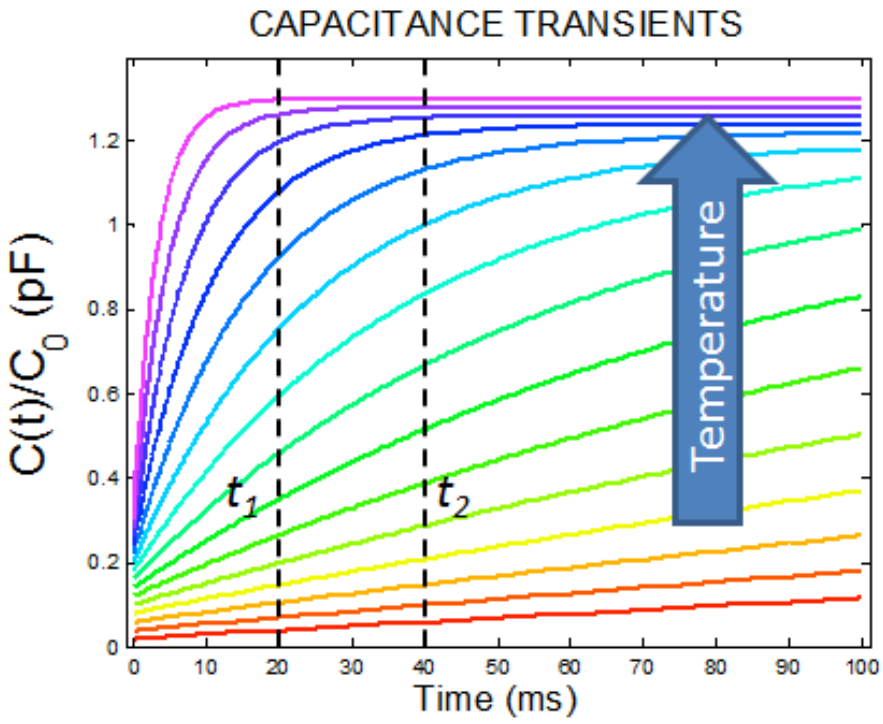

Figure 3.6: Example of a capacitance transient obtained during C-DLTS measurements

The C-DLTS setup includes a capacitance meter, a voltage source and a temperature-controlled plate on which to place the device. The procedure consists of two phases:

- The voltage source applies the filling voltage $V_{filling}$ for a specific time $t_{filling}$ to ensure the filling of available traps
- The voltage source applies a reverse voltage V_R while the capacitance meter records the capacitance transient.

In order to measure a more precise capacitance value, it is mandatory to left the capacitance value return to the steady state one, after turning off the light inside the probe station.

3.3.2 Deep Level Optical Spectroscopy (DLOS)

Deep Level Optical Spectroscopy is used to find and identify also deep levels with high activation energy. These defects cannot be revealed by classical the DLTS technique because they cannot be thermally activated without destroying the device with an extremely high temperature. However, the drawback with this technique is the added complexity and time required for the measurements.

During the Deep Level Optical Spectroscopy, at a certain time t, the device is illuminated with a monochromatic light source with the intent of excite electron and holes trapped in the deep levels and so observe a variation in the junction capacitance. Depending on the nature of the traps, the capacitance can increase or decrease: a positive variation of the capacitance corresponds to an emission of majority carrier while a negative variation corresponds to the emission of minority carriers from the deep levels. When the device capacitance reaches a steady-state value the light is turned off leaving the capacitance free to return to the initial value. This measurement can be repeated with the device biased at different voltages, to investigate the variation of junction capacitance in the presence of different active and barrier regions.

During the measurement, the band diagram of, for example, a p^+n junction with majority carrier trap in the n-side will follow these five phases:

- When, initially, the light is off, the capacitance is at its steady state value because both the donors and the trap states located above the quasi-Fermi level of the n side are empty (the depletion region edge is where the empty donors ends);
- When the light is turned on, it will start to excite some electrons that will eventually be captured by the empty donor near the conduction band. In order to maintain charge neutrality, the quasi-Fermi level increases and so the space-charge-region (SCR) will shrink leading to an increase of the junction capacitance;
- After some time the system reaches steady state regime and the capacitance does not increase more;
- When the light is turned off, more and more traps will start to capture electrons and more donors will be ionized to maintain neutrality. The capacitance will therefore decrease butm since this phenomenon depends on the trapping mechanism of the deep levels, it will happen during a long period of time with a dynamic dependent on the trapping characteristic of the defects;
- After some more time the initial steady-state value is restored and the measurement can be repeated in different conditions.

The monochromatic light is typically generated by a quartz-halogen lamp and a monochromator. The light is then focused on the device by some lenses and is turned on and off by a remote controlled shutter. The measurement involves the use of different wavelengths of the incident light in order to excite trapping and de-trapping processes in deep levels with different activation energies. In Figure 3.8 it is possible to observe a typical curve obtained during a DLOS measurement, for a specific wavelength.

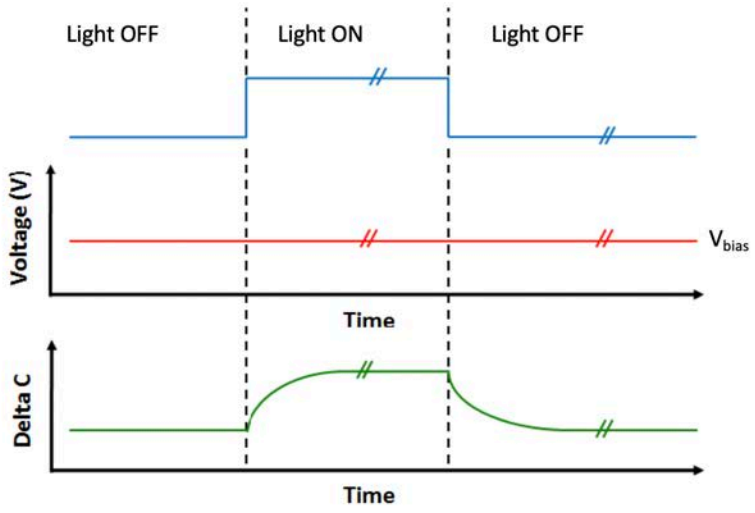

Figure 3.7: Schematic representation of the various phases of a DLOS measurement

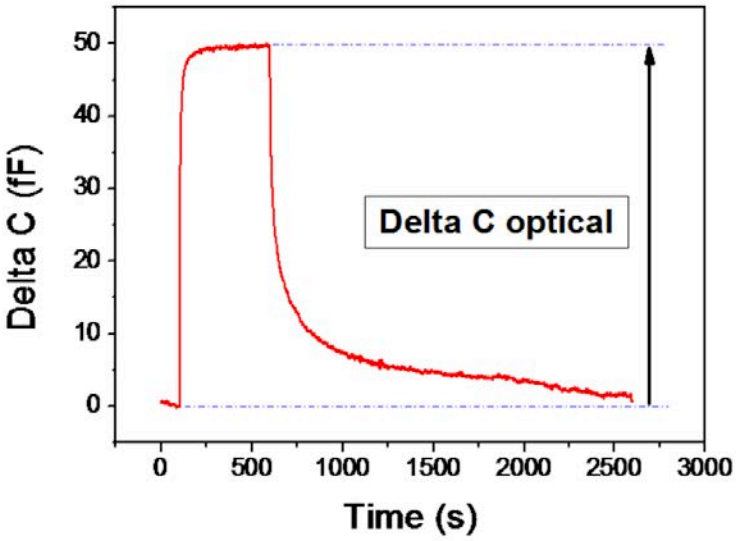

Figure 3.8: Example of a single DLOS transient at a specific wavelength of incident light

Usually this technique can be exploited to perform two different types of analysis: the first is the spectral dependence of the Steady-State Photo-capacitance (SSPC) which permits to estimate the trap density N_t and the second is the spectral dependence of optical cross-section (PCS) which helps to find the optical ionization energy required for a photon to promote an electron or a hole.

To obtain the SSPC spectrum we need to plot ΔC or $\Delta C/C$ as a function of the photon energy measured in eV. In Figure 3.9 an example of SSPC spectrum can be seen: every change of slope in these spectrum points to the onset of the emission of carriers from a new type of deep level. Therefore, this change in slope can be used to identify the type of deep level present.

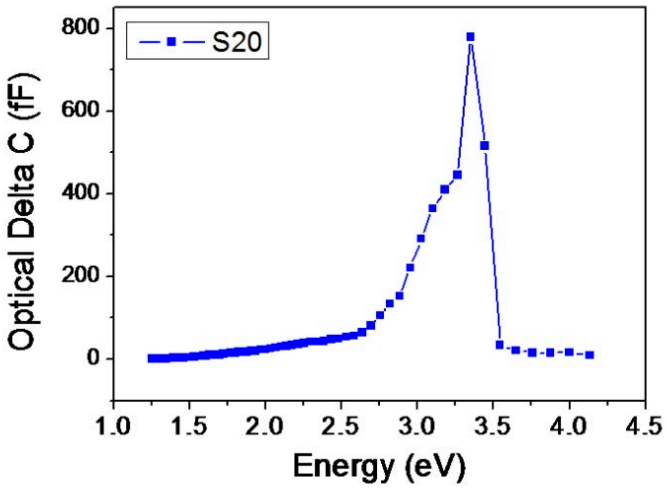

Figure 3.9: Example of a SSPC spectrum

Starting from the obtained capacitance transient, the concentration of traps for a n-type semiconductor can be calculated as follows:

$$\frac{\Delta C}{C} \cong \frac{N_t}{2N_d} \frac{\sigma_n}{\sigma_n + \sigma_p} \tag{3.3}$$

where N_d is the donor concentration and σ_n and σ_p are the two cross-sections for electrons and holes. Normally this equation is evaluated for the energy value which has the strongest photo-capacitance response.

On the other hand with the PCS it is possible to obtain the optical ionization energy E_o and the Franck-Condon energy d_{FC} which, however, will not be calculated in our analysis.

4

Polarization-doped vertical GaN diodes

Impurity doping in wide band-gap semiconductors has prove to be very inefficient, mainly due to the high activation energy of positive-charge carriers (holes) coming from, for example, Mg in gallium nitride.

It is possible to avoid this problem with polarization-induced doping, which exploits the spontaneous and piezoelectric polarization fields already present in III-V nitrides to produce both p- and n-type doping. In particular, an abrupt heterojunction can create a sharp discontinuity in the field and so generate a thin sheet of charge at the interface. This charge creates a high electric field and a bending of the energy-bands such that a two-dimensional electron gas (2DEG) is created at the hetero-interface, without the need of dopants. Such 2DEG is the foundation of GaN-based High Electron Mobility Transistors (HEMT) that have outperformed transistor made from any other material, in RF applications.

If instead of a sharp junction we grow a graded crystal slowly passing from GaN to AlGaN, a similar phenomenon takes place, with the difference that the resulting charge will spread also along the third axis and so inducing the formation of a mobile 3D carrier gas. This gas will be composed of electron in case of a Ga-face crystal and hole in case of a N-face crystal. The resulting carrier slabs are created by the ionization from the electrostatic field and so are quite different from those formed by impurity doping. In particular, these slabs have higher conductivity than impurity-doped slabs of comparable carrier concentration, thanks to the absence of impurity scattering [15].

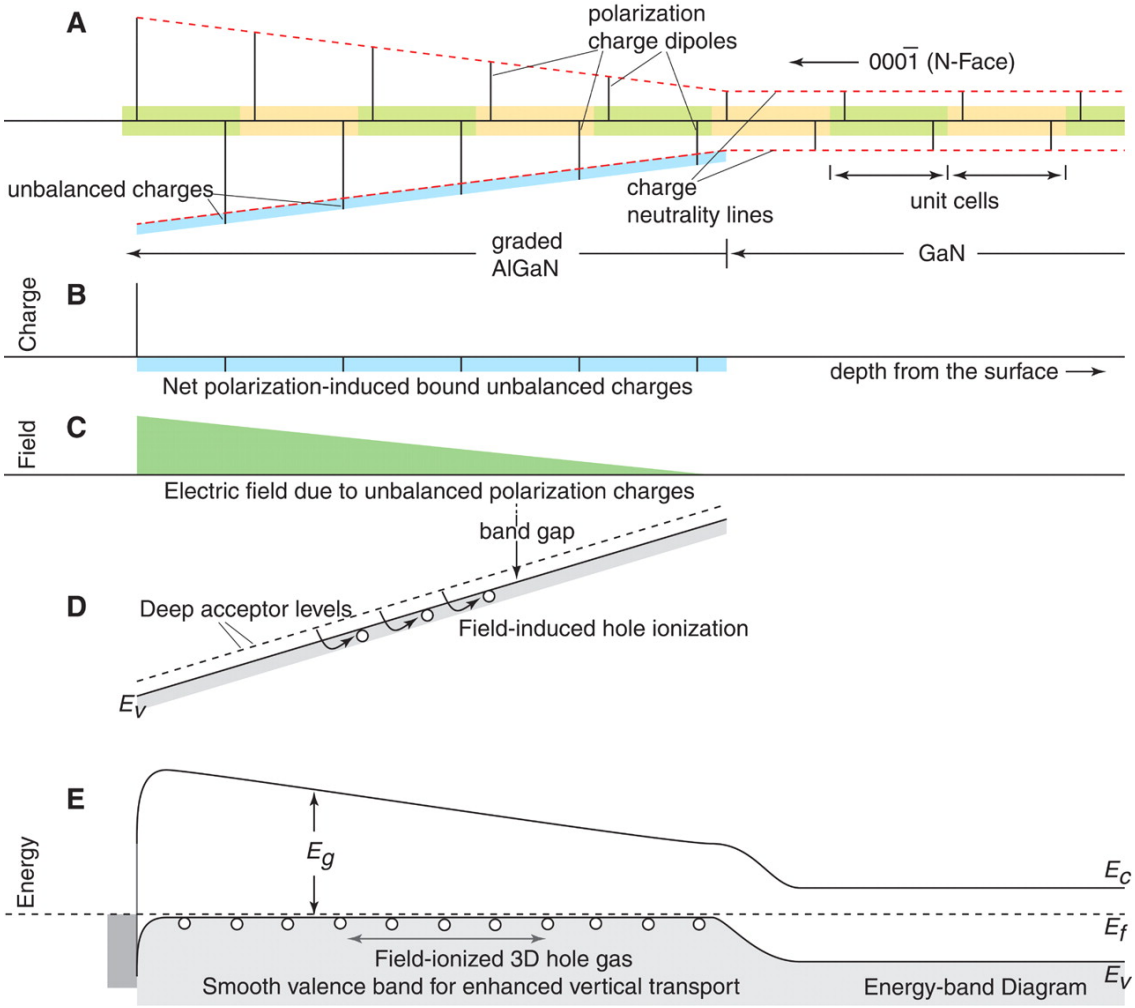

Figure 4.1: Schematic illustration of polarization-induced p-type doping

In Figure 4.1 it is possible to see a schematic representation of how polarization doping works. The graded AlGaN will create a polarization-induced sheet of charge which spreads along the entire AlGaN volume. The resulting charge is showed in section A as single dipoles positioned every crystal unit cell and the resulting unbalanced charge is showed in section B. This charge leads to the creation of an electric field which can ionize holes from deep Mg-acceptor atoms and so create a 3D hole gas under the valence band, as can be see in the steady-state energy band diagram, visible in section E.

With this technique, it is therefore possible to obtain highly conductive wide-band-gap structure with higher concentration of carriers, in comparison to impurity doping. These devices also tend to have higher breakdown voltage, thanks to the larger band-gap of AlGaN, and they will not suffer of carrier freeze-out. This freeze-out is avoided because, in polarization-doped devices, free carriers are activated by the polarization field and not by temperature. These carriers are expected to have also faster dynamic response, thanks to the avoidance of heavy use of magnesium as a deep acceptor.

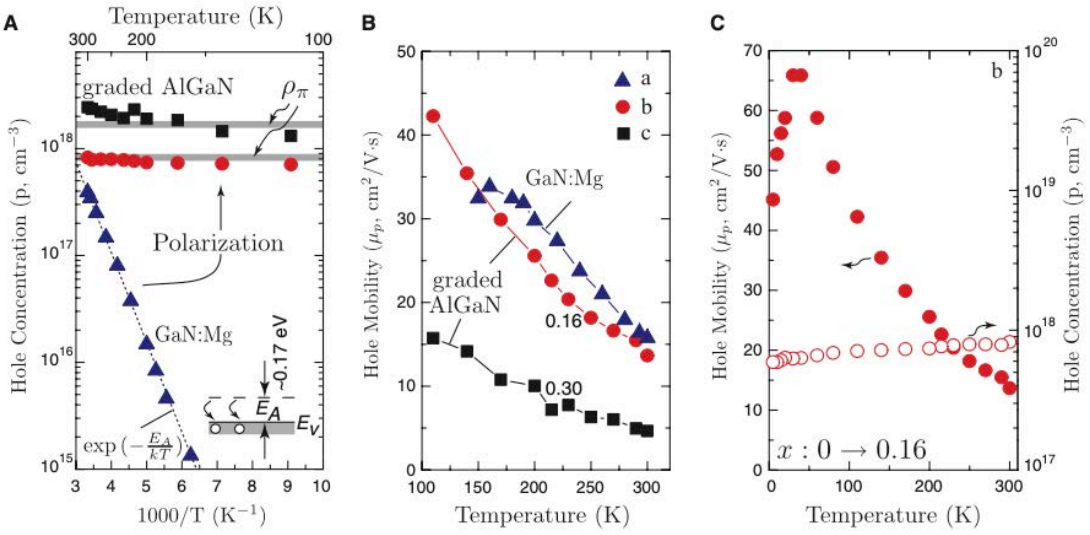

Figure 4.2: Comparison of hole concentration and mobility of polarization-doped and Mg-doped diodes [15]

4.1 Device specifications

The tested devices were two generations (Gen1 and Gen2) of polarization-doped p-n vertical GaN diodes.
The wafers of the two generations, visible in Figure 4.3, were composed of 4 identical cells.

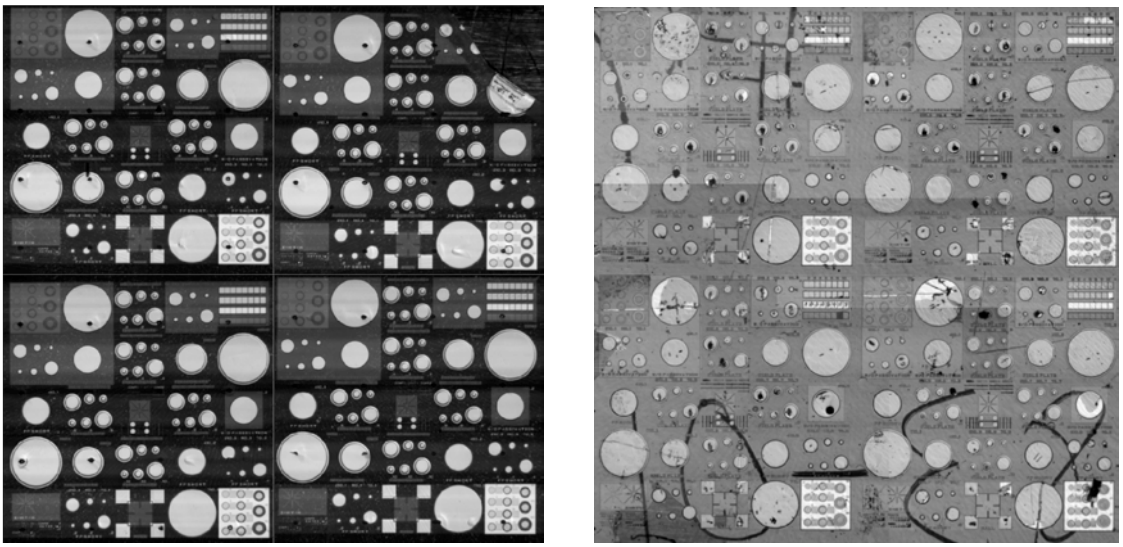

Figure 4.3: Photos of the wafers of polarization-doped vertical diodes: Gen1 on the left and Gen2 on the right

Each cell contains multiple diodes of different dimensions and with different field plate geometries. In figure 4.4 it is possible to see how the various geometries and dimensions are distributed inside each cell. The diameters of the various devices are 70 μm, 110 μm, 210 μm, 410 μm, and 710 μm.

Some of these devices were optimized for high breakdown voltages through the use of different geometry of field plates: every device is therefore available with long, short or without the field plate. For everyone of these geometries, a top view and x-section can be seen in Figure 4.5.

Both generations share the same basic structure with the only structural difference being the substrate on which they were manufactured: the first generation was grown on b-dot core GaN substrate and the second generation was grown on Hitachi Grade B GaN substrate.

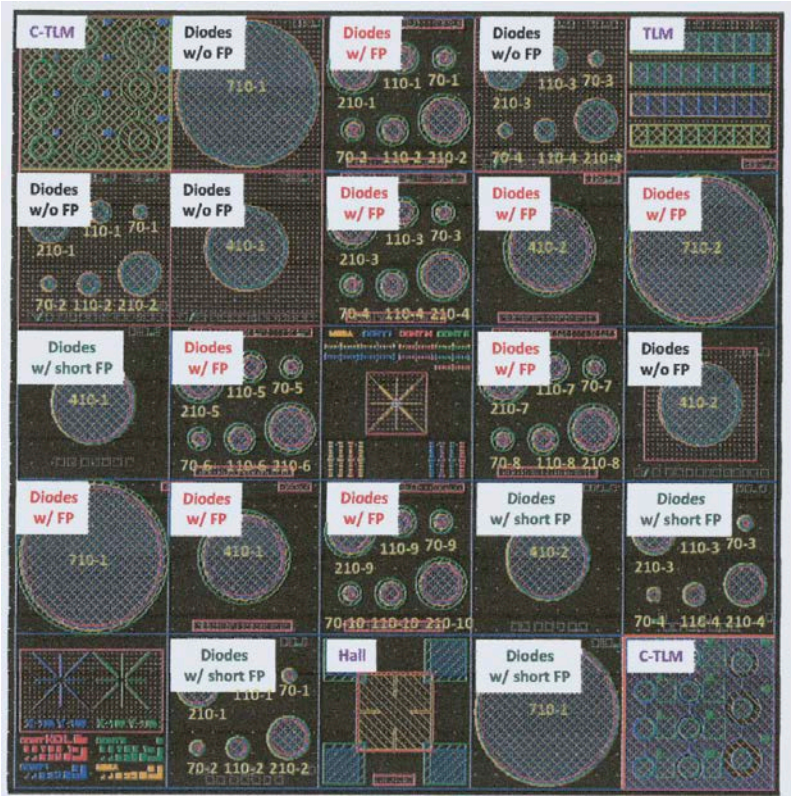

Figure 4.4: Mask of a single cell of devices

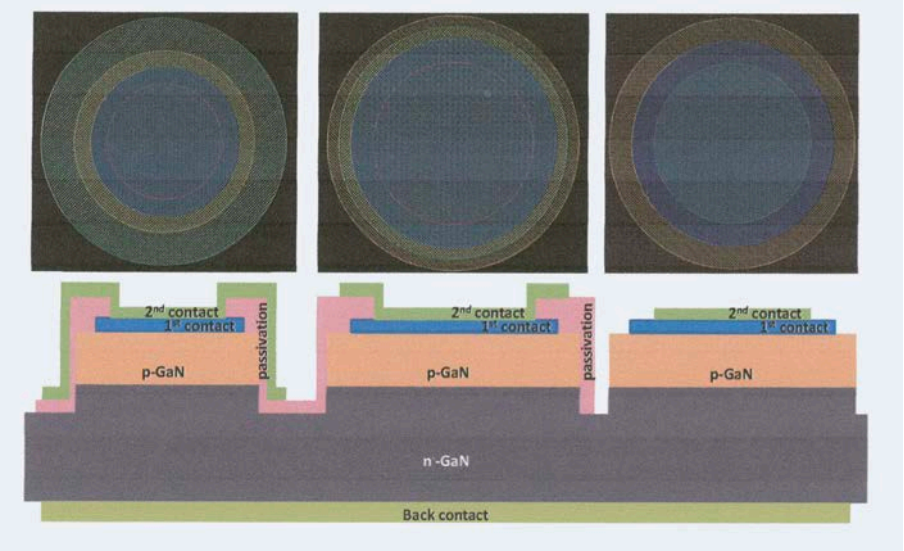

Figure 4.5: Structure of the different field plate geometries

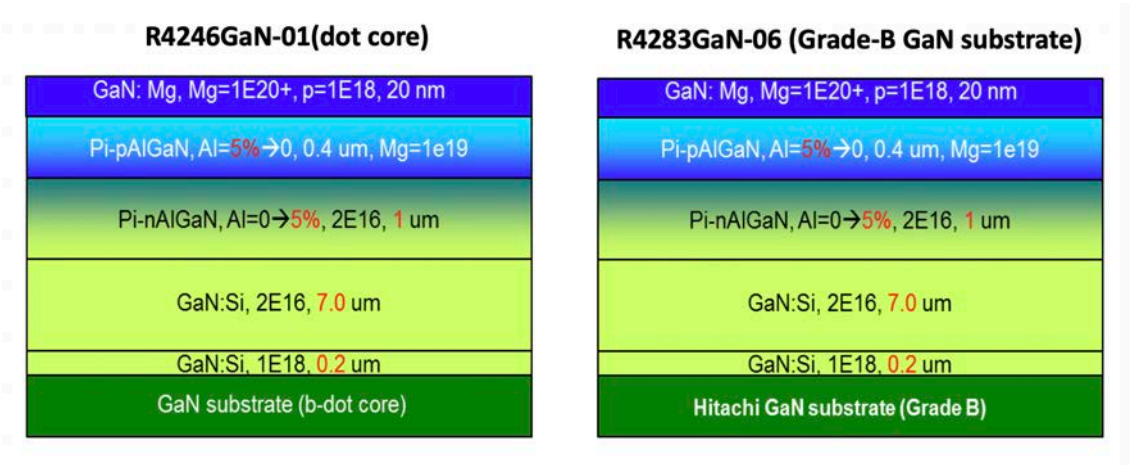

Figure 4.6: Structures of the two generation of tested polarization-doped vertical diodes

All devices consist of (from top to bottom):

- A Mg-doped p-GaN layer of 20 nm with doping higher than 10^{20} cm^{-3};
- A 0.4 μm thick p-type AlGaN layer, linearly graded with Al composition going from 5.6% to 0%. In this layer magnesium was used as dopant in order to provide the free charge necessary to balance the polarization induced charge field;
- A 1 μm thick AlGaN layer with n-type doping and opposite grading of Al.
- A Si-doped n-GaN layer of 7 μm with $N_D \sim 2x10^{16}$ cm^{-3};
- A Si-doped n^--GaN layer of 200 nm with $N_D \sim 1x10^{18}$ cm^{-3};
- A bulk substrate of GaN.

In these devices no intentional carbon doping was added, but residual concentration was detected afterwards. In particular, SIMS data, reported in Figure 4.7, show a much higher concentration of carbon in the first generation compared to the second generation.

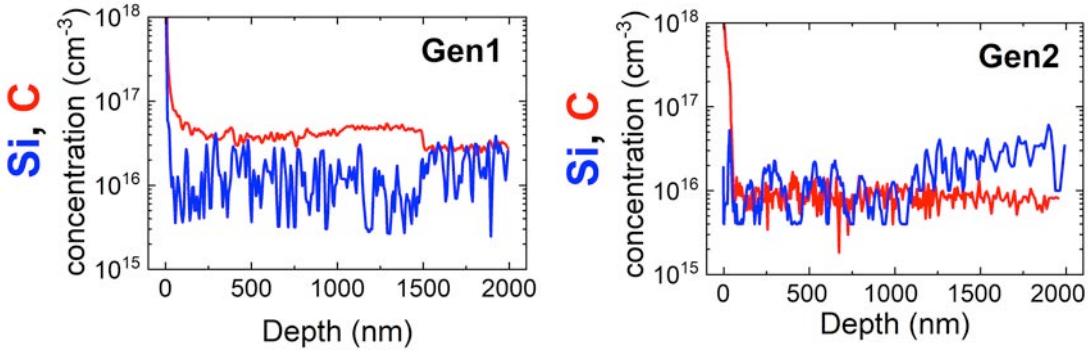

Figure 4.7: Silicon and carbon concentrations in devices of both generations obtained from secondary ion mass spectrometry (SIMS) measurements

Since this different carbon concentration is the only difference between the two generations, comparing the results obtained from them could help us to study how the presence of carbon can affect the performance and the reliability of GaN polarization-doped devices.

4.2 Role of carbon in avalanche regime

This thesis work is the continuation of the analysis carried out on the same devices and already reported in the literature [16]. In particular, an I-V characterization under reverse bias, at different temperatures, was realized. These measurements have proven the avalanche capability of these polarization-doped diodes, which is highly desirable for the development of high-voltage devices.

During these characterizations, the two generations have shown different behaviors. In particular, as can be seen in Figure 4.8, first generation devices have higher breakdown voltage and lower leakage than second generation devices. Both generations presented positive temperature coefficients with a slopes of $0.54\,V/°C$ for the fist generation and $0.27\,V/°C$ for the second generation. This is due to the fact that a lower carbon concentration results in a non-optimal compensation of the drift region, with consequences on the electric field spatial distribution.

Moreover, the two generations showed a different behavior of the reverse voltage in avalanche

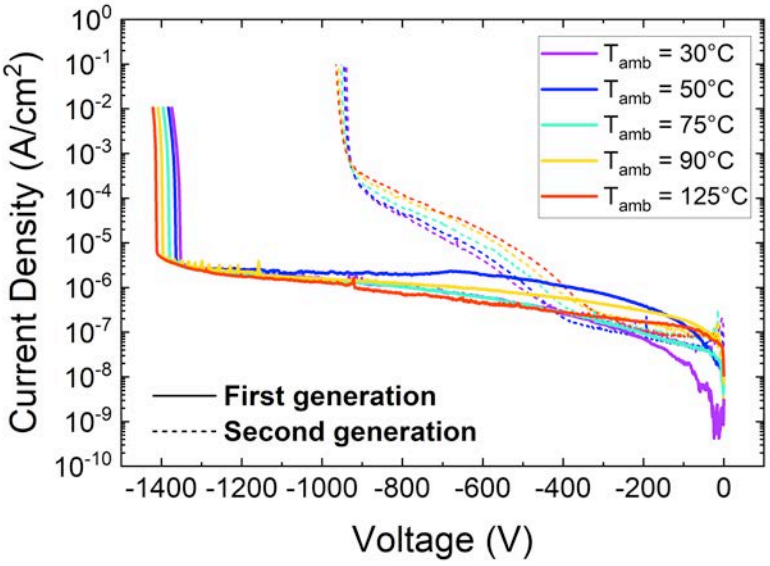

Figure 4.8: I-V characteristics at different temperatures and dependence of the breakdown voltage on the temperature for both generations

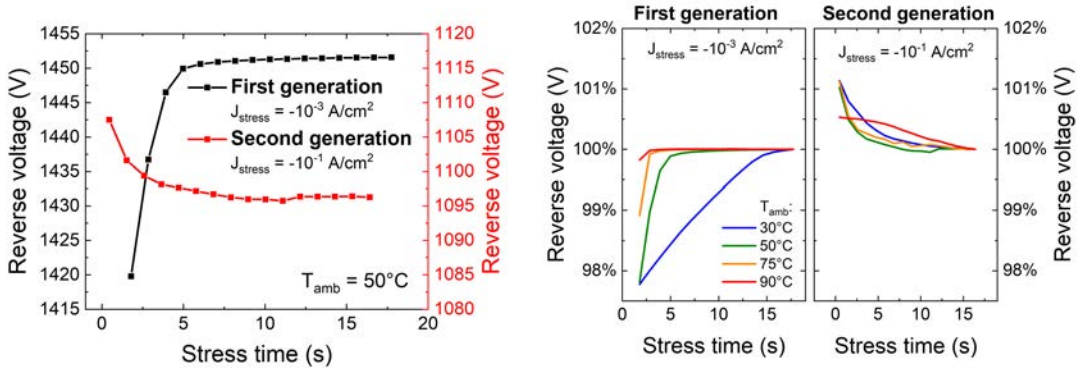

Figure 4.9: Time-dependence of breakdown voltage at different temperatures for both generations

regime: the breakdown voltage increased during a constant current stress under avalanche mode in the devices of Gen1, indicating the presence of breakdown walkout, whereas it decreased in Gen2. In addition, Gen2 devices had a smaller variation of the breakdown voltage, indicating better stability during avalanche operations, probably due to the lower concentration of carbon. In fact when a high negative bias is applied, carbon impurities start to capture electrons. This leads to a decrease in the mean-free path, with a consequent increase in the voltage required to trigger impact ionization [16].

From this characterization, we were able to confirm that the different carbon concentration in the two generations can indeed affect their performance and reliability. For these reasons, further analysis on the influence of carbon on these devices has been carried out.

4.3 Deep Level characterization

To deeply investigate the impact of carbon on the behavior of the devices, a series of more advanced measurements was carried out.

As mentioned in chapter 3, the most relevant techniques used to characterize deep levels are the Capacitance Deep Level Transient Spectroscopy (C-DLTS) and Deep Level Optical Spectroscopy (DLOS).

4.3.1 C-DLTS Measurements

Capacitance Deep Level Transient Spectroscopy measurements were carried out only on devices of the first generation.

Initially, on the device, a filling pulse of $V_{filling} = 0\,V$ and duration of $10\,s$ was applied, in order to fill the defects in the depletion region. After this pulse, we measured, for 1200 seconds, the de-trapping capacitance transient, while biasing the device at different $V_{measure}$. By using different voltages, it was possible to analyze different active regions of the device. We then repeated all these measurement at different temperatures in order to extract the Arrhenius plot and so calculate the activation energy of the traps. Before every measurement, we waited at least 1800 seconds in order to let the device stabilize from the previous measurement.

We carried out two sets of measurements: in the first $V_{measure}$ was varied from $-0.5\,V$ to $-40\,V$ (employing an LCR meter) and the measurement was repeated at $300\,K$, $308\,K$, $313\,K$, $318\,K$, $328\,K$ and $343\,K$ for each voltage, the second set was carried out by using the B1505, up to $V_{measure}$ of $-100\,V$, and the measurements were repeated at $308\,K$, $323\,K$ and $333\,K$.

Examples of resulting capacitance transients for both sets of measurement can be seen in Figure 4.10.

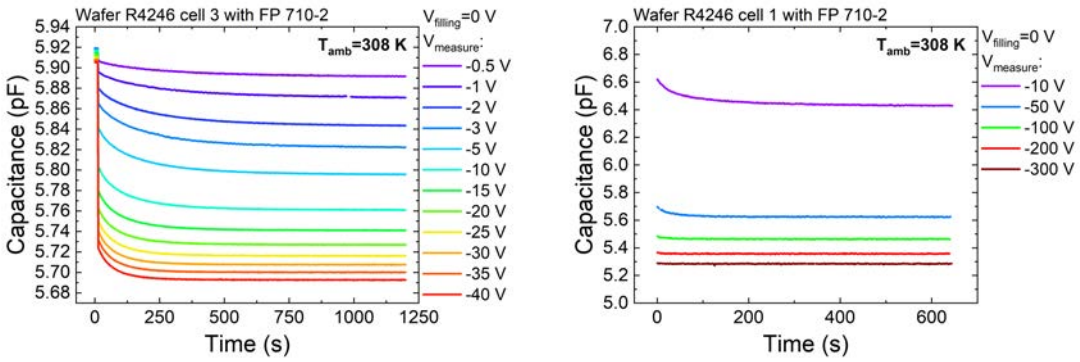

Figure 4.10: Examples of C-DLTS capacitance transients

From these transients, it is possibile to see that with higher negative voltages the amplitude of the capacitance (proportional to the number of deep levels) increases, indicating that the transients are due to a minority carrier trap [17].

In order to characterize the deep levels responsible for the observed capacitance variation, we realized the measurement also at different temperatures. With the time constants extracted from a stretched exponential fit of these transients, we were able to obtain the Arrhenius Plot reported in Figure 4.11, which contains the results of both sets of measurements.

The comparison of the data obtained from the C-DLTS analysis with previous papers [18] [19] [20] [21], visible in Figure 4.12, confirms the presence of carbon on nitrogen sites (C_N) in these devices.

From the slope of the curves in the Arrhenius plot, we were able to extract the activation energy E_a at different voltages, for both sets of measurements.

We can note that the data of the two sets of measurements matches quite well and that with higher reverse voltages the activation energy increases and tends to stabilize around a value of 0.85 eV. This is probably caused by the fact that with different voltages we are investigating dif-

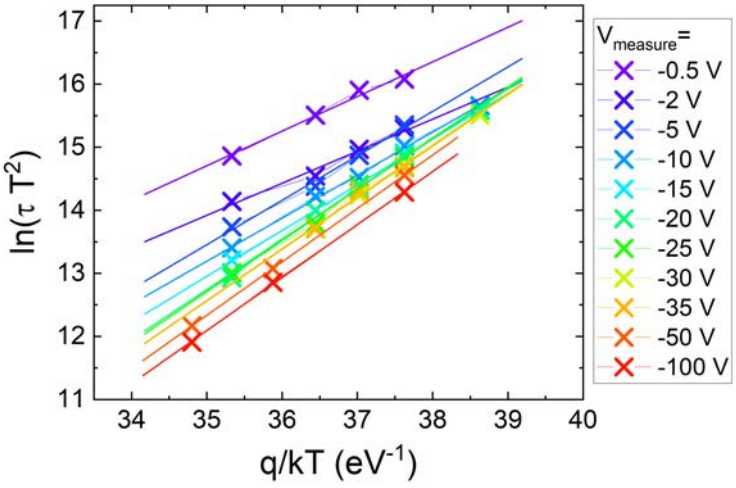

Figure 4.11: Arrhenius plot obtained from C-DLTS measurements at different voltages

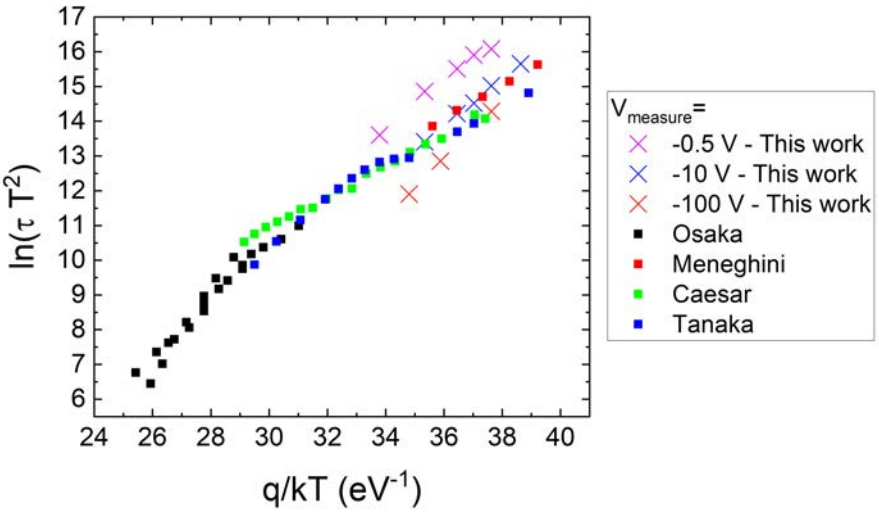

Figure 4.12: Comparison between literature and some of the Arrhenius plots obtained from C-DLTS measurements

ferent regions of the device. In particular, it is possible that with the increasing applied voltage we are moving toward a region in which the carbon concentration is lower and where defect-assisted tunneling is less probable. In this region the obtained activation energy is in fact close to the expected value for carbon defects. On the contrary, at lower voltages, carbon defects are

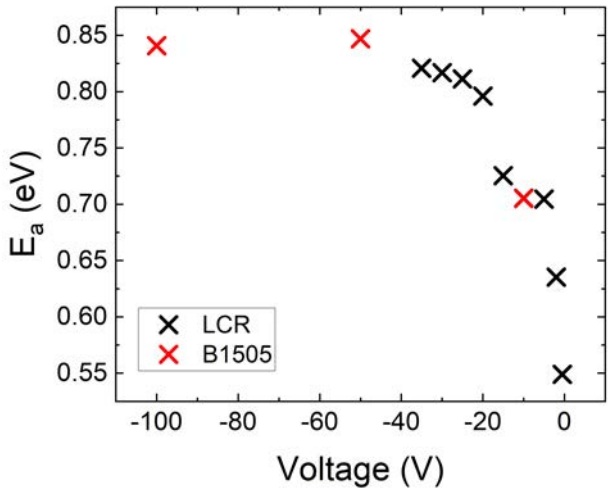

Figure 4.13: Activation energy with respect to $V_{measure}$ for both sets of measurements

enhancing the defect-assisted emission mechanisms resulting in a lowered activation energy.

Additionally, from the data obtained from these C-DLTS measurements, we were also able to estimate the trap density N_t and the donor density N_d, and plot their dependence on the voltage, at different temperatures.

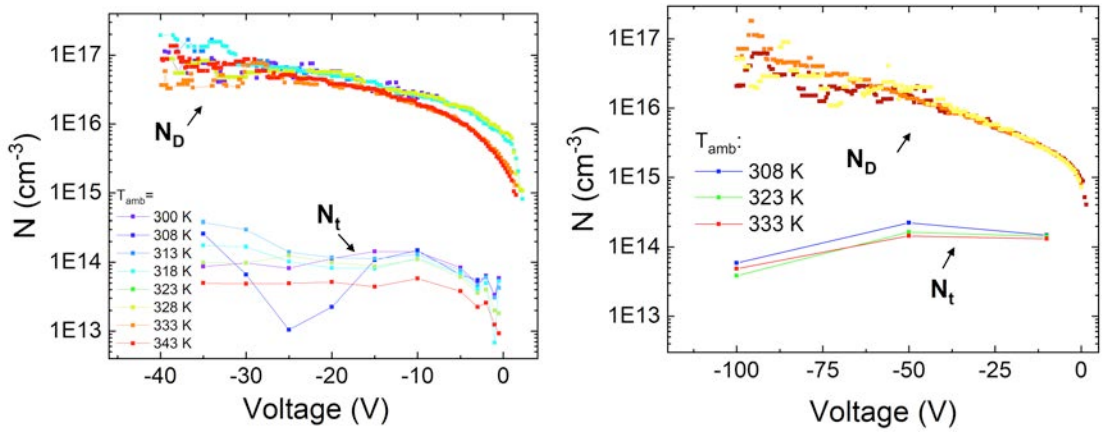

Figure 4.14: Donor and trap densities with respect to the applied voltage, for both sets of measurements

4.3.2 DLOS Measurements

We performed DLOS measurements in order to further characterize the presence of carbon in both generations of devices.

In DLOS measurements the capacitance transient is monitored while a light is turned on and then off. In particular, when the light is on, traps will emit carriers by absorbing photons and so causing a variation in the capacitance of the junction. When the light is turned off, an opposite transient is registered as the capacitance returns to the initial value.

Before every measurement we waited for 100 second to let the device stabile. After these period, the light is turned on and the capacitance transient si monitored. After 300 seconds the light is turned off again and the capacitance is let to return to the steady-state value.

In order to investigate how carbon can affect the behavior of the devices at different bias voltages, the measurements were repeated starting from $0\,V$ up to the failure with a step of $-50\,V$. To monitor the variation in the activation energy of carbon in different polarization conditions, we used a monochromatic light with photon energies between $2\,eV$ and $3.2\,eV$.

First Generation

Two sets of measurements were carried out on devices of the first generation: the first using a LCR meter, with V_{bias} varied from $0\,V$ to $-40\,V$, and the second using the B1505 Power Device Analyzer with V_{bias} varied from $0\,V$ to $-450\,V$, with a step of $50\,V$.

Two of the resulting capacitance transients for both measurements sets can be seen Figure 4.15.

From these transients, we were able to extract the $\Delta C/C$ by analyzing the variation between the value of capacitance during the first 100 seconds of dark and the maximum capacitance value reached with the light on. From the resulting $\Delta C/C$ transients, we extracted the maximum value $\Delta C/C_{max}$. We were therefore able to plot the Steady-State Photo-Capacitance (SSPC)

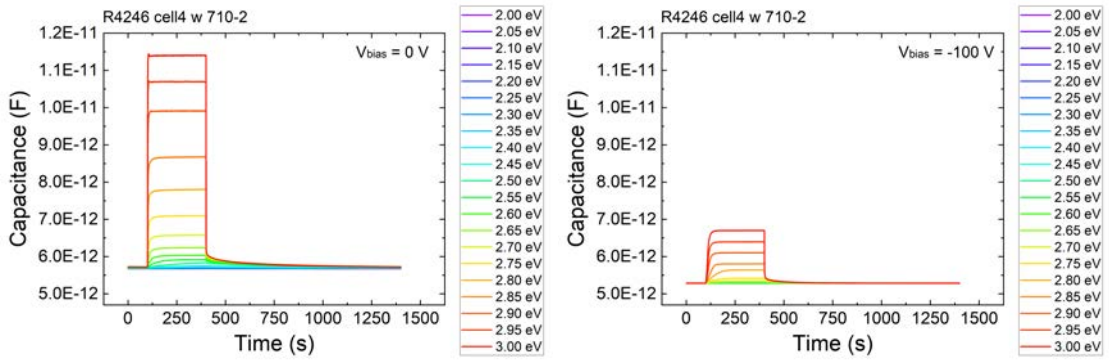

Figure 4.15: Example of capacitance transients acquired during DLOS measurements on Gen1 devices with the B1505

spectrum, i.e. the $\Delta C/C_{max}$ variation with respect to the photon energy, at the various voltages.

In Figure 4.16 is reported the SSPC spectrum of the second set of measurements, both in linear and in semi-logarithmic scale.

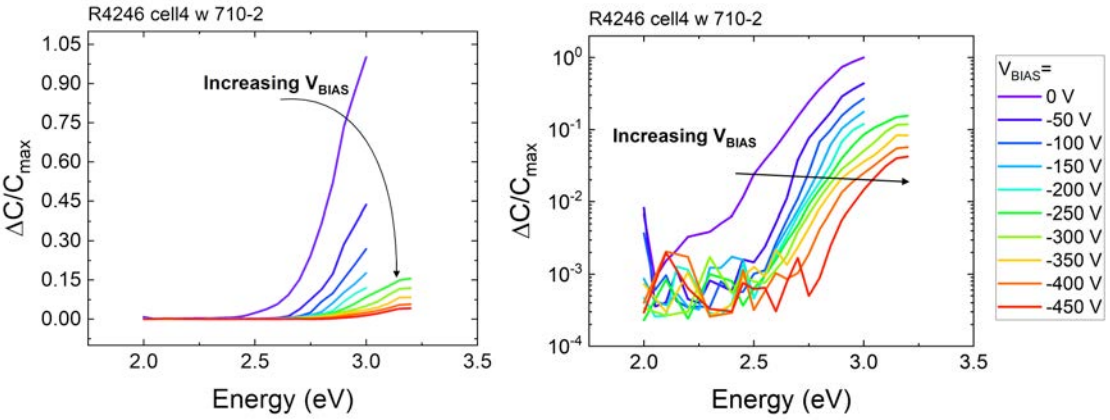

Figure 4.16: SSPC spectrum of Gen1 devices from $0\,V$ to $-405\,V$ in linear scale on the left and in semi-logarithmic scale on the right

From the linear version of the SSCP, we can extract the change in slope, of all the curves. This change in the slope is indicating the start of an emission process of carrier from deep levels.

It is therefore possible to calculate the energy of the emission process by subtracting the energy

at which the slope changes at the energy gap of the material, i.e. $3.4\,eV$

$$E_{emission} = E_G - E_{change\ slope} \tag{4.1}$$

The resulting values for the energy of the emission process can be seen in Figure 4.17.

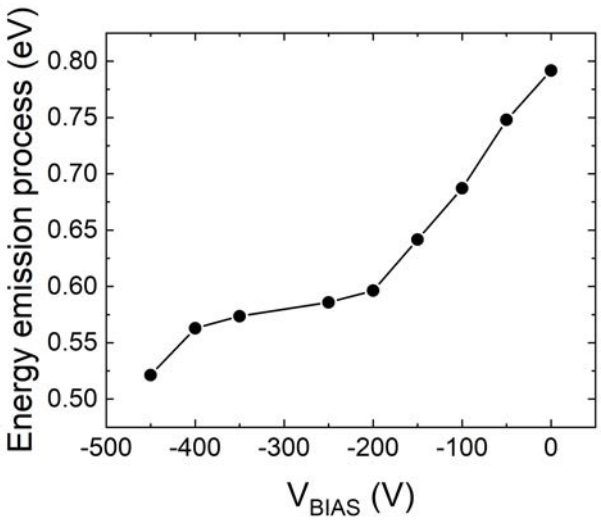

Figure 4.17: Energy of the emission process with respect to the applied voltage

The obtained energy of $0.9\,eV$ at $0\,V$ is consistent with the value for substitutional carbon defects [13].

At higher negative voltages we can see a decrease in the energy of the emission process. This behavior is probably due to the Poole-Frenkel effect, which consists of an enhancement of the emission rate in presence of an electric field [14]. In particular, the bending of the energy band due to the presence of such electric field enhances various transport mechanisms, resulting in a lowered required energy for the carrier to escape from the trap.

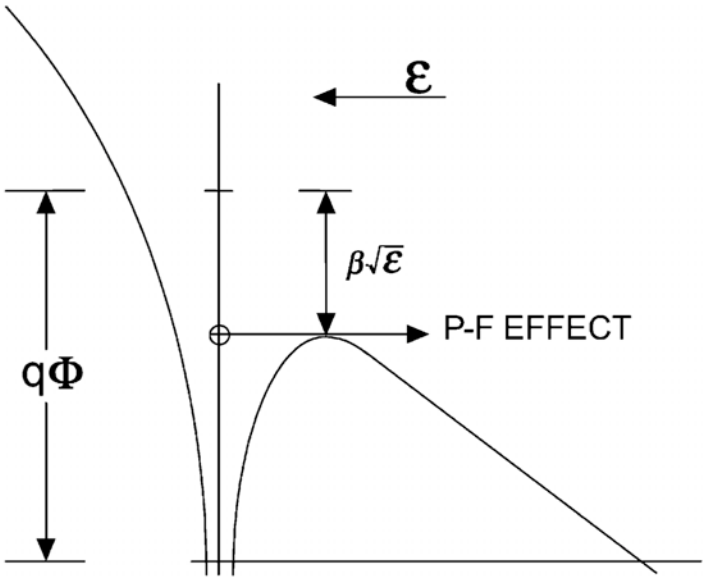

Figure 4.18: Potential well in presence of an electric field illustrating the Poole–Frenkel effect

Second generation

For the measurements on Gen2 devices we used a V_{bias} varied from $0\,V$ to $-250\,V$; some of the resulting capacitance transient can be seen Figure 4.19.

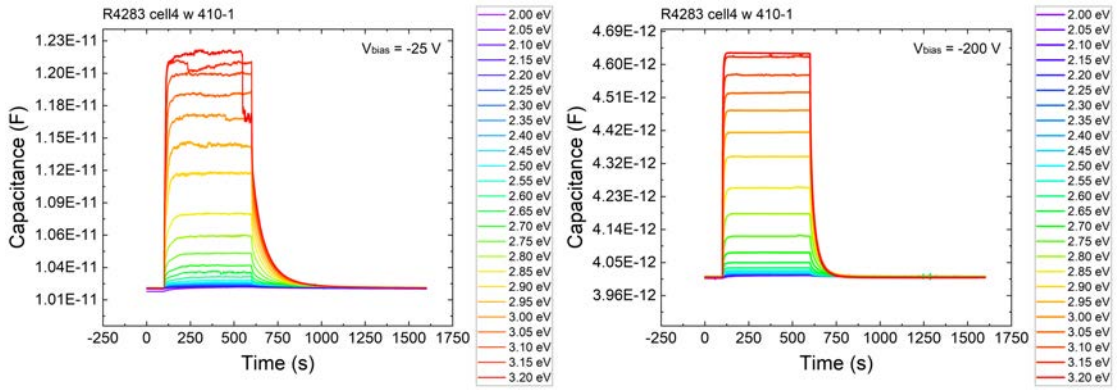

Figure 4.19: Example of capacitance transients acquired during DLOS measurements on Gen2 devices

The obtained transients were inconsistent and unreliable, so repeating these measurements is highly required to validate the obtained results.

As for the first generation, we extracted the maximum $\Delta C/C$ in order to plot the SSPC spectrum both in linear and in semi-logarithmic scale.

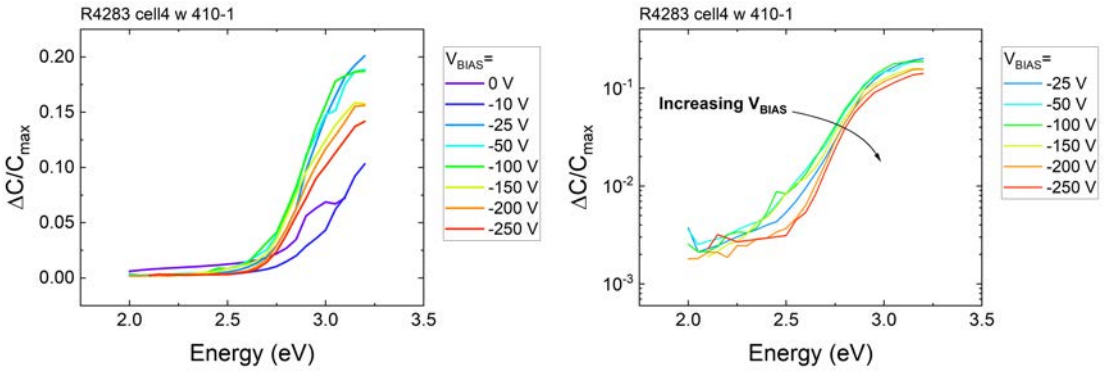

Figure 4.20: SSPC spectrum of Gen2 devices from $0\ V$ to $-405\ V$ in linear scale on the left and in semi-logarithmic scale on the right

Due to the low reliability of the data obtained from the measurement on devices of the second generation, we were not able to extract the change of slope in the SSPC spectrum and so calculate the energy of the emission process. For this reason, the measurement on the second generation devices need to be repeated.

4.4 Optical and electrical characterizations at cryogenic temperatures

To deeply characterize the role of carbon in the devices, we carried out electrical and optical analysis under different temperature conditions.

The used setup includes the aforementioned cryogenic probe, equipped with a stage capable of reaching temperatures between 50 and 650 K, a Compact Array Spectrometer (CAS) and a Keysight 4155 Semiconductor Parameter Analyzer. The latter was used to keep the device under a constant current condition in order to measure the emitting light, and also to carry out I-V measurements.

We carried out these characterizations for both generations of polarization-induced diodes and also for an impurity-doped GaN-on-Gan vertical diode.

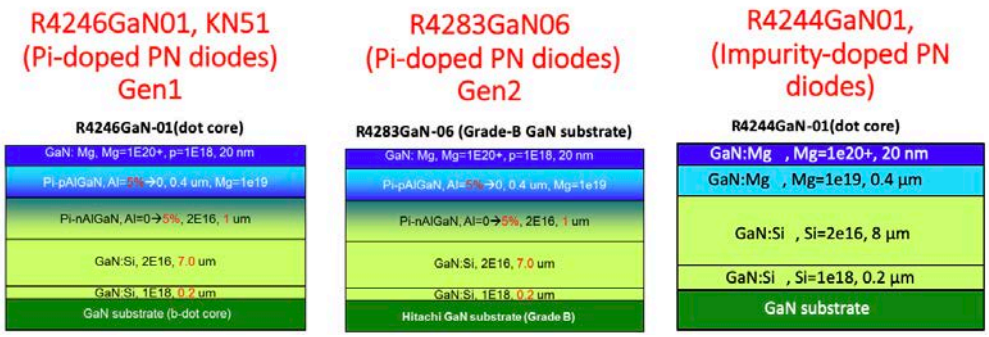

Figure 4.21: Structures of the three tested devices: Gen1 on the left, Gen2 in the middle, and impurity-doped diode on the right

In Figure 4.21, a comparison between the structures of the three tested devices is presented. The first and the second generation of devices share an identical structure except for the substrate and the carbon concentration. The impurity-doped diodes have a similar structure, with the main difference being the absence of AlGaN, which is used to achieve polarization-doping. In Figure 4.22 is possible to see the concentrations of carbon, silicon and aluminum in the three sets of devices.

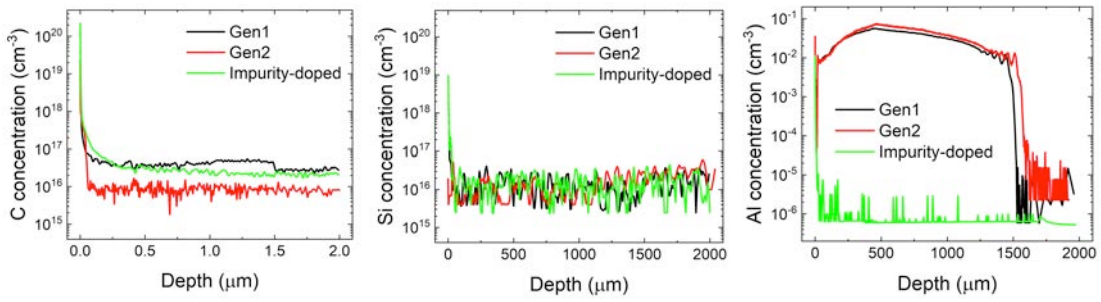

Figure 4.22: SIMS data for the concentrations of carbon, silicon and aluminum for the three teste devices

The analysis was composed of a constant current stress (220 seconds) during which the emission spectrum was acquired from the CAS, with 3 average and an integration time of 60 seconds. Every spectrum was repeated at different current values and, during these stresses, the voltage was monitored to evaluate the self-heating of the device. Before and after every set of spectral acquisitions, I-V measurements were performed in order to determine if the constant current stress induced a degradation of the devices.

4.4.1 I-V characterization

Before and after every spectra acquisition, we carried out I-V measurements from $-10\,V$ to $6\,V$, to characterize the general behavior of the various devices at different temperatures.

The resulting I-V characteristics at some temperatures, for all three tested devices, can be seen in Figure 4.23 in linear scale and in Figure 4.24 in semi-logarithmic scale.

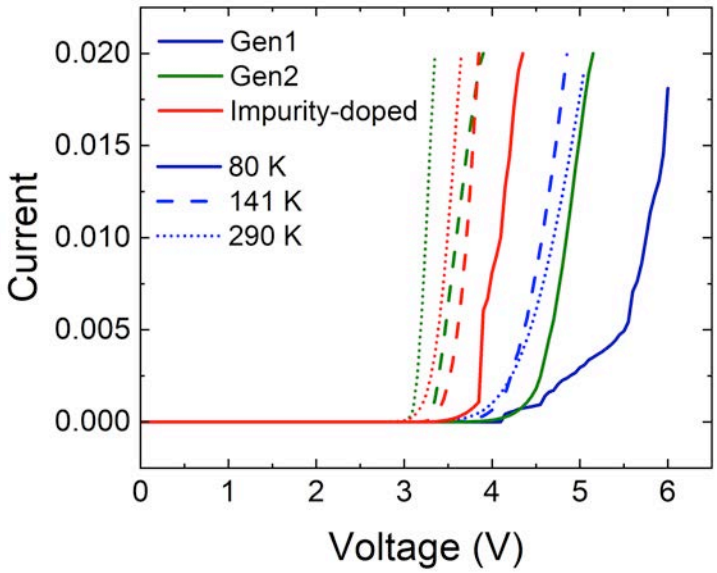

Figure 4.23: Comparison of the I-V characteristics of the three tested devices in linear scale

We can note that the first generation of polarization-doped diodes and the impurity-doped diodes show a hump in the I-V characteristic at low temperatures ($80\,K$, $100\,K$ and $120\,K$). This phenomenon could be related to higher carbon concentration of these two wafers (see Figure 4.22) which can lead to a different compensation of the n-type doping.

From the obtained I-V characteristics we analyzed also the behavior of the series resistance, which can be seen in Figure 4.25. We can observe that Gen1 and Gen2 have opposite temperature-dependence on the series resistance: in Gen1 the resistance increases with temperature and vicev-ersa for Gen2. The impurity-doped diode shows a lower variation of the series resistance than the two polarization-doped diodes.

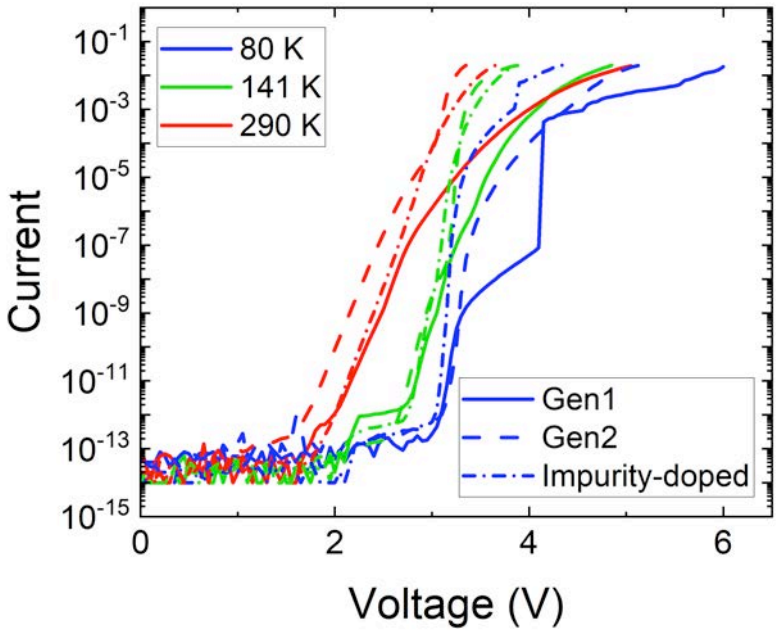

Figure 4.24: Comparison of the I-V characteristics of the three tested devices in semi-logarithmic scale

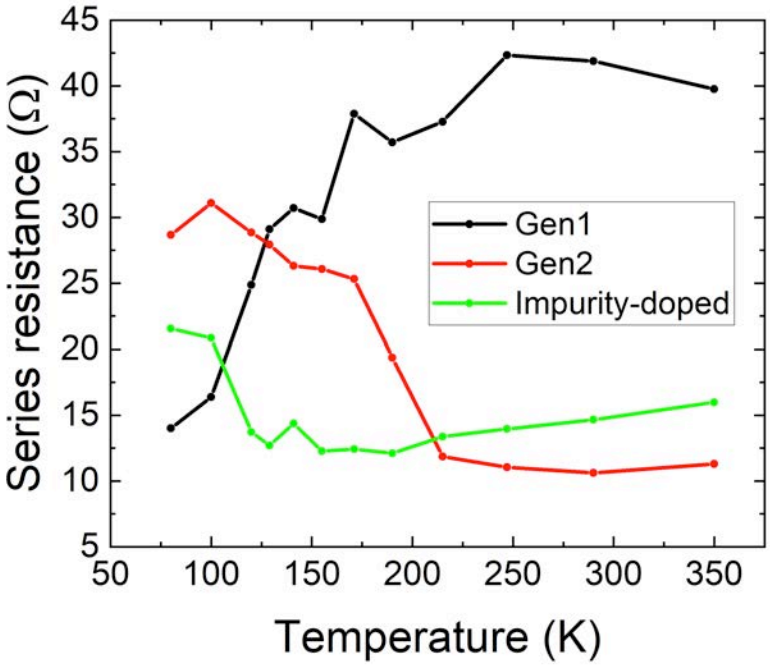

Figure 4.25: Series resistance with respect to temperature for all three tested devices

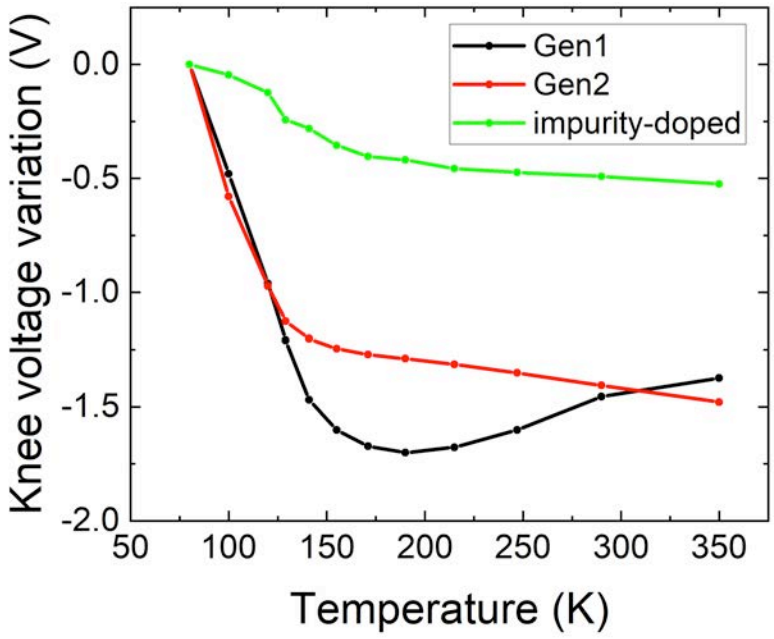

Figure 4.26: Knee voltage variation with respect to temperature for all three tested devices

We also analyzed the behavior of the knee voltage (the forward voltage at which the current starts to increase rapidly) at different temperatures, which can be seen for all three diodes in Figure 4.26. In particular, we can note the non-monotonic trend of the voltage with respect to the temperature for the Gen1 device. On the other hand, Gen2 and impurity-doped diodes showed a negative shift on the knee voltage with increasing temperature. Additionally, the impurity-doped diode has showed a smaller variation of the voltage than both polarization-doped diodes.

4.4.2 Photoluminescence characterization

In order to characterize the optical behavior of the devices, we acquired the emission spectrum under different constant current conditions. An example of the obtained spectra for Gen1 devices at 80 K, from 350 nm to 700 nm, can be seen in Figure 4.27.

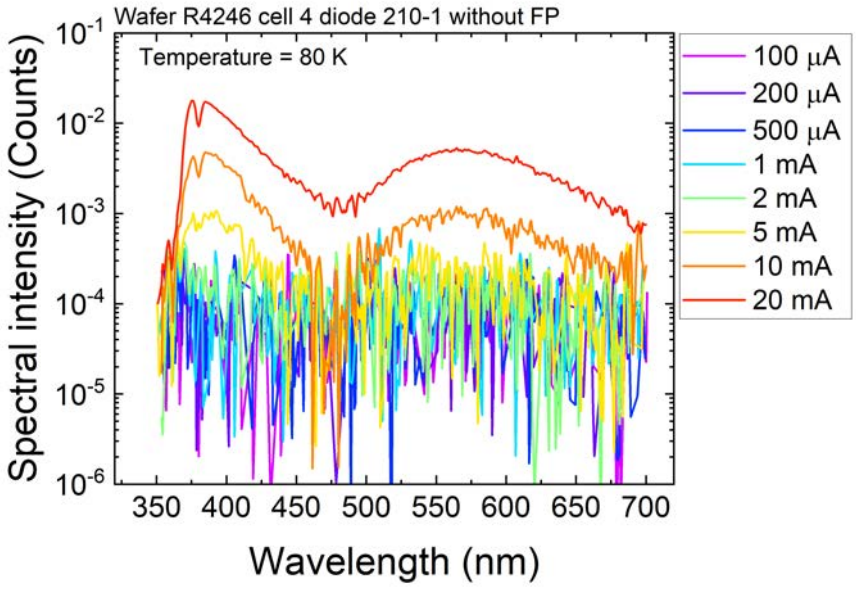

Figure 4.27: An example of spectra obtained from the photoluminescence characterization

No assumptions can be made on the absolute intensity of the emission due to manual fiber alignment which could have lead to a different positioning and so a different acquired optical power for the various devices.

In Figure 4.28 all the spectra obtained at 20 mA are plotted for different temperatures, for all three devices.

From these graphs we can recognize some photoluminescence band typical of Gallium Nitride [22].

The yellow luminesce (YL) band, located roughly at 2.15 eV, was already reported in literature and was attributed to a transition from a shallow donor to a $C_N - V_{Ga}$ (substitutional carbon and gallium vacancy) deep acceptor complex [23]. As expected this band is broad and increases with temperature in all the devices [22].

Also the blue luminescence (BL) band, located roughly at 2.9 eV, has already been found in heavily doped GaN with concentrations of Mg above 10^{19} cm^{-3}, like all three of our devices [22].

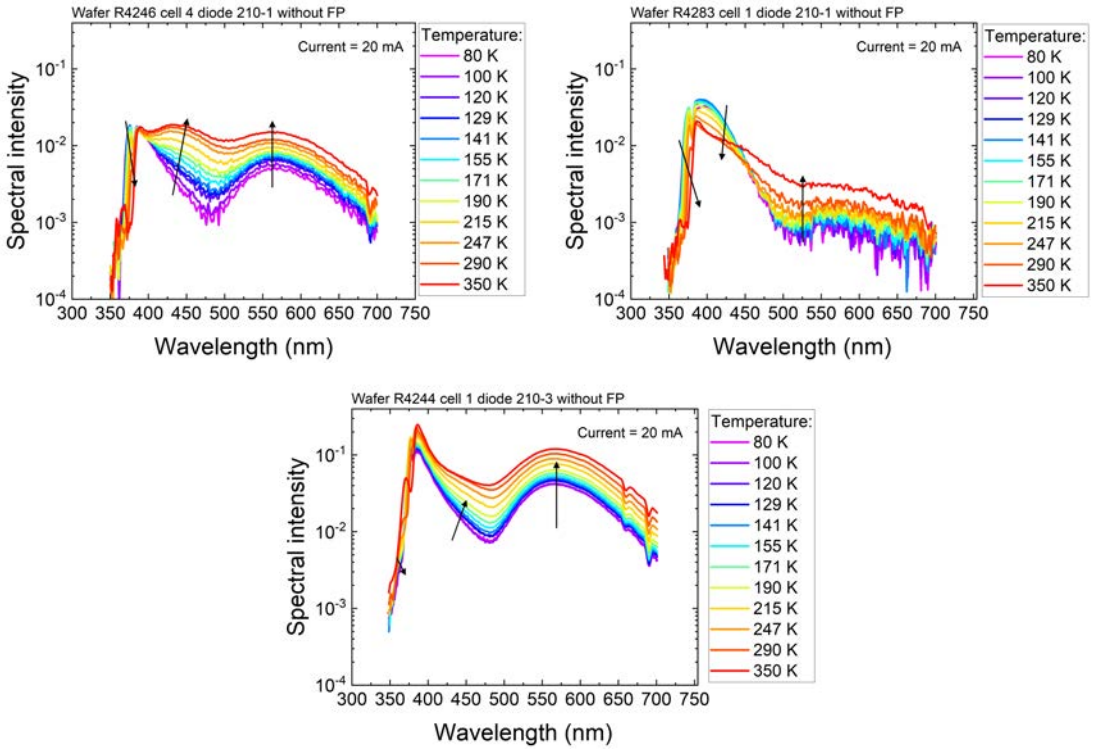

Figure 4.28: Spectra obtained with a constant current of $20\ mA$ for tested devices

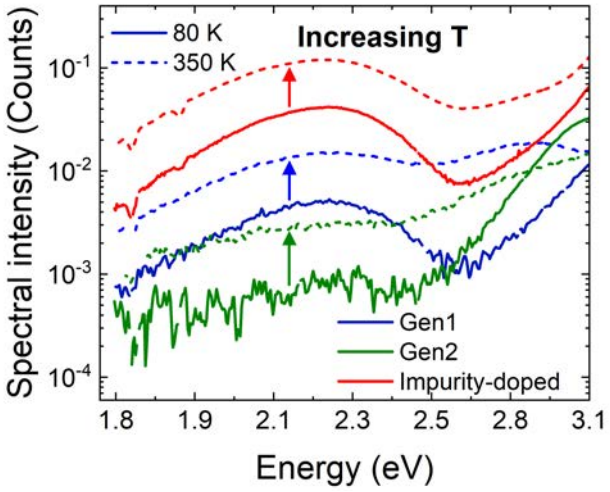

Figure 4.29: Comparison of the behavior of the yellow luminescence band in the tested devices

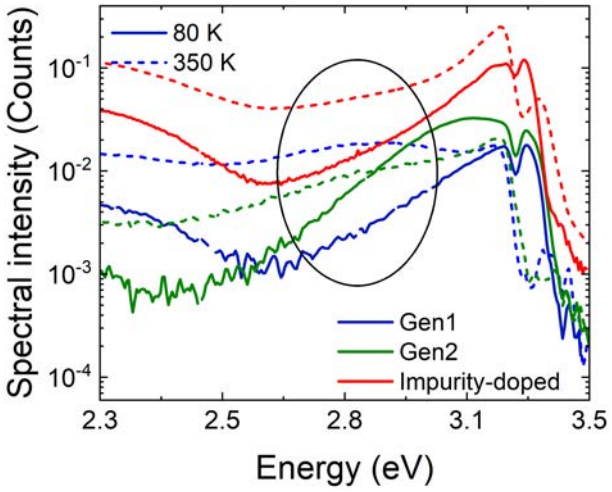

Figure 4.30: Comparison of the behavior of the blue luminescence band in the tested devices

This band increases with temperature only in the devices with higher carbon concentration (Gen1 and impurity-doped) suggesting that carbon defects could be one of the causes of this luminescence, as was already theorized [13].

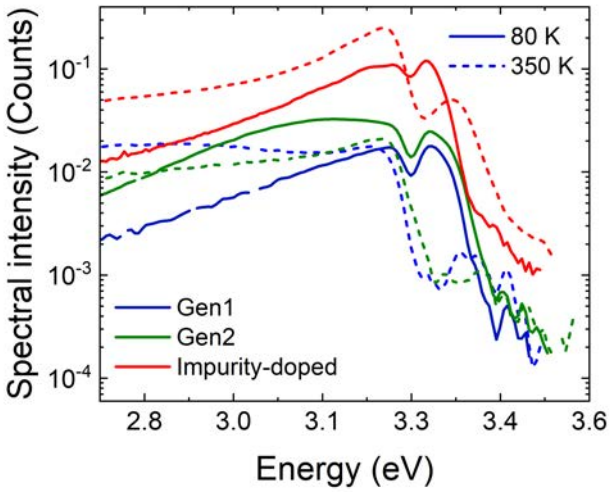

Figure 4.31: Comparison of the behavior of the UV luminescence band in the tested devices

In addition to the BL band, the photoluminescence spectrum of heavily Mg-doped GaN usually shows a strong enhancement of the UV luminescence (UVL) band, so presenting a rela-

tively sharp peak at about 3.26 eV [22]. This peak is present in all our devices and it decreases slightly with increasing temperature in both generations of polarization-induced diodes but it increases in impurity-doped diodes.

Another narrow peak centered a roughly 3.35 eV is present (see Figure 4.31) and it increases with increasing temperature in all the devices. This near-band-edge luminescence could be linked to the presence of activated Mg [24].

5

GaN/AlN based Resonant Tunneling Diodes (RTDs)

Tunneling junctions and devices are quite used in a wide range of applications such as oscillators or amplifiers.

At first glance, Gallium Nitride may seem not optimal for achieving inter-band tunneling due to its very large band-gap (3.4 eV) and to the difficulty in achieving highly doped p-type GaN. However, the polarization-induced electric field that we discussed in chapter 4, present at the AlGan/GaN or InGaN/GaN interface, can enable the required alignment of the bands and so allow tunneling.

Tunneling is a phenomenon in which a particle can pass through a potential barrier having an energy lower than the barrier itself. In addition to classic tunneling, a variety of tunneling pro-

cesses can be identified. In particular, resonant tunneling is exploited for building microwave oscillators or to inject electrons with a precisely controlled energy in vertical unipolar devices such as quantum cascade lasers or resonant hot electron transistors. The devices capable of delivering these types of behavior are called resonant tunneling diodes (RTDs) and are usually based on double-barrier heterostructure of III-V semiconductors. In these diodes, the current flow reaches a local maximum when the energy of electrons coming from the emitter is in resonance with an adjacent reservoir of electrons, giving the name to these devices.

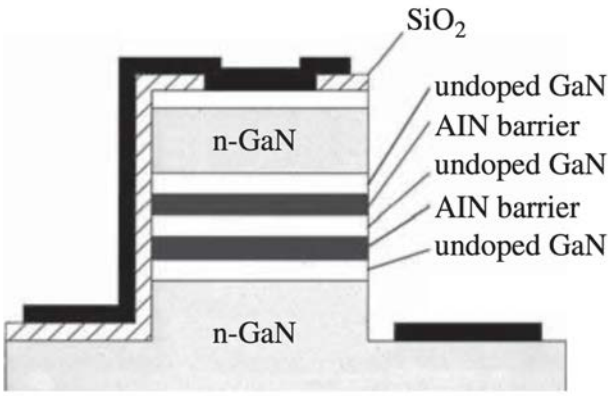

Figure 5.1: Typical structure of a GaN RTD

A typical GaN/AlGaN RTD, reported in Figure 5.1, consists of a very thin (0.5-2 nm) GaN quantum well positioned between two thin AlGaN barriers (1-3 nm) and two n-type doped GaN contact layers. The double heterostructure is required because in the case of a single heterostructure the transmission coefficient is less than one for the entire height of the barrier. For double-heterostructure instead, it is possible to achieve a transmission coefficient equal to one even if the incident electron has less energy than the two barriers. This phenomenon is called resonant tunneling and brings a Negative Differential Conductance (NDC) section in the I-V curves, which can be very useful to achieve for example microwave oscillation (THz).

Resonant tunneling and NDC have been extensively investigated in arsenide heterostructure [25], but only recently have been demonstrated at room temperature (RT) for GaN/AlGaN based devices [26].

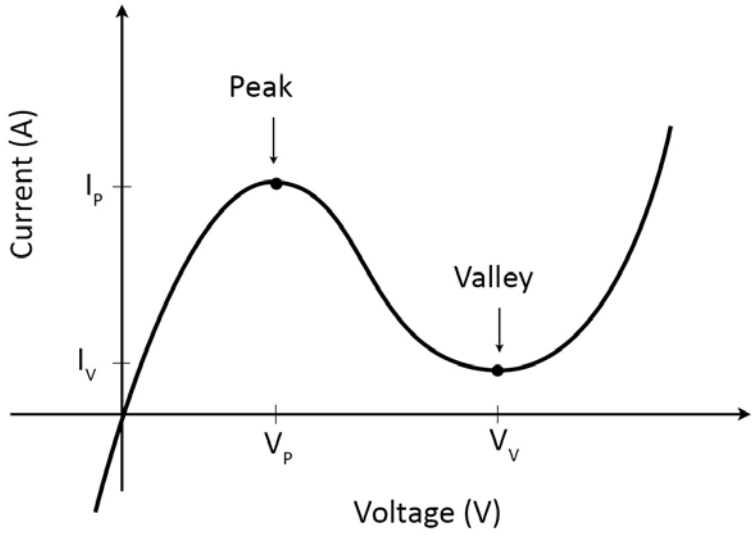

Figure 5.2: Typical I-V characteristic of Resonant Tunneling Diodes

As can be seen in Figure 5.2, the I-V characteristic of this type of devices is strongly influenced by the resonant tunneling phenomena. A peak in the current is present at the resonant voltage, which is achieved when the bands are bent enough to align with the quasi bound state inside the well and so create a permitted path through the barrier. In figure 5.3 it is possible to see how, at the resonant voltage, the bands are aligned with the permitted path of the well so that the maximum transmission coefficient is achieved. For further increase of the bias, the tunnel current flow decreases as the allowed path moves away from the energy level of the electrons. The minimum of the total current, called valley current, is determined by leakage, scattering, and thermionic current flow. After this valley, the current increases with an exponential trend, which is consistent with thermionic emission over the double-barrier.

In principle, AlGaN/GaN double-barrier diodes offer advantages such as material robustness, high breakdown field, and large conduction-band discontinuity. However, the asymmetric band diagram induced by the presence of the polarization fields at the interfaces is a challenge for the design of RTDs in nitride semiconductors. Preliminary devices showed asymmetric I−V characteristics due to the presence of defects and dislocations acting as traps or leakage

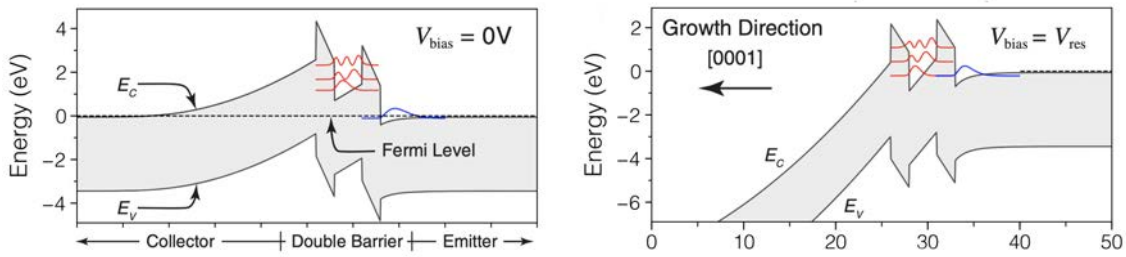

Figure 5.3: Schematic band diagram of a resonant tunneling diode, both at 0 V and at the resonance voltage

path, making the realization of resonant tunneling difficult, especially if fabricated on foreign substrates [27].

The improvement in vertical GaN devices fabrication allowed the manufacturing of devices with lower defects densities, which permit GaN-based RTDs to achieve repeatable NDC at room temperature [28].

5.1 Devices specifications

The tested resonant tunneling diodes were grown by MBE on commercially available single-crystal bulk n-GaN substrate with dislocation density under $5\,x\,10^4\,cm^{-2}$. Metal-rich conditions were maintained during the epitaxy to minimize the roughness of the epitaxial layers.

The devices were distributed on multiple cells all containing a complete set of RTDs with areas of $18\,\mu m$ x $18\,\mu m$, $16\,\mu m$ x $16\,\mu m$ and $14\,\mu m$ x $14\,\mu m$ (other smaller devices were present but have not been tested). At the center, a big rectangular ground pad was also present.

The device structure contains two 100 and $200\,nm$ respectively thick n-GaN layers, doped degenerately with silicon donors with a nominal concentration of $\sim 6 \cdot 10^{19}\,cm^{-3}$, which acts as contact electrodes. Intrinsic spacers were also included next to the contact layers to minimize dopant diffusion into the barriers region. These spacers were positioned asymmetrically to reduce the extension of the collector depletion region next to the top contact. The active region

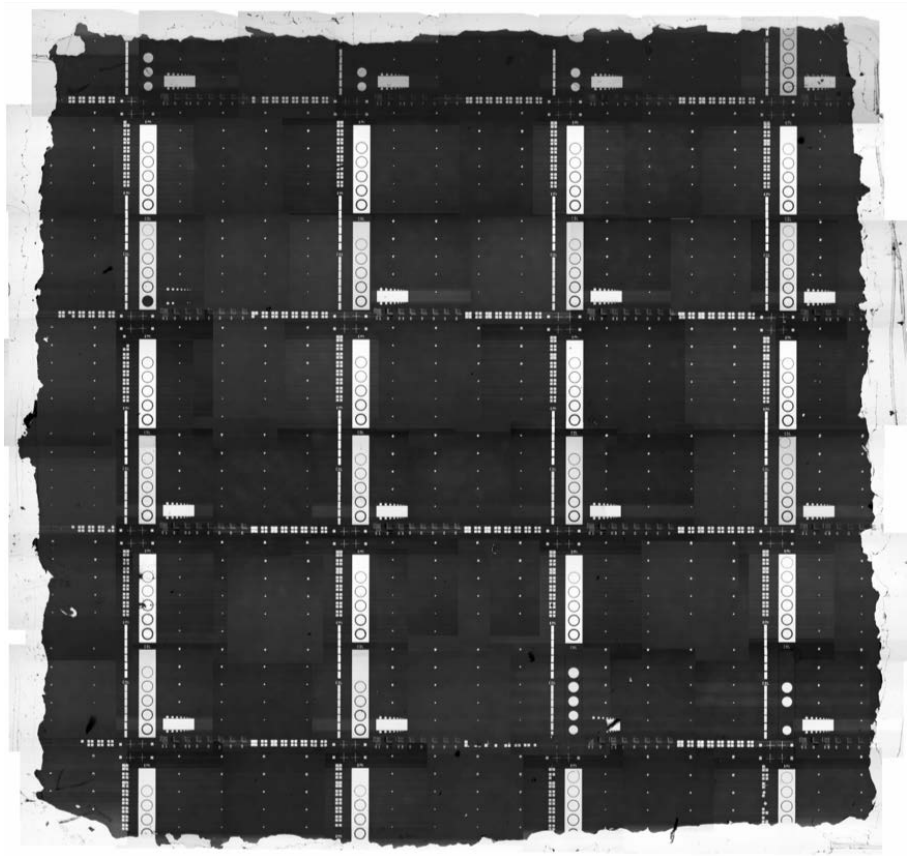

Figure 5.4: Photo of the entire wafer of resonant tunneling diodes

is formed by two AlN barriers of $\sim 2\,nm$ around a $3nm$ thick GaN quantum well.

Usually a structure with symmetrical barriers is desirable but in the polar case the situation is the opposite: in fact, at zero bias condition, the conduction band profile E_c is strongly asymmetric and so resulting in a reduced transmission coefficient. Under forward bias, however, the bands can align and so produce symmetric configuration. Usually, this condition is obtained close to the resonant voltage.

5.2 Preliminary characterization

As a first analysis, we have carried out a preliminary DC characterization on 15 different devices: we tested devices of all 3 dimensions across 5 different test structures. This would help us

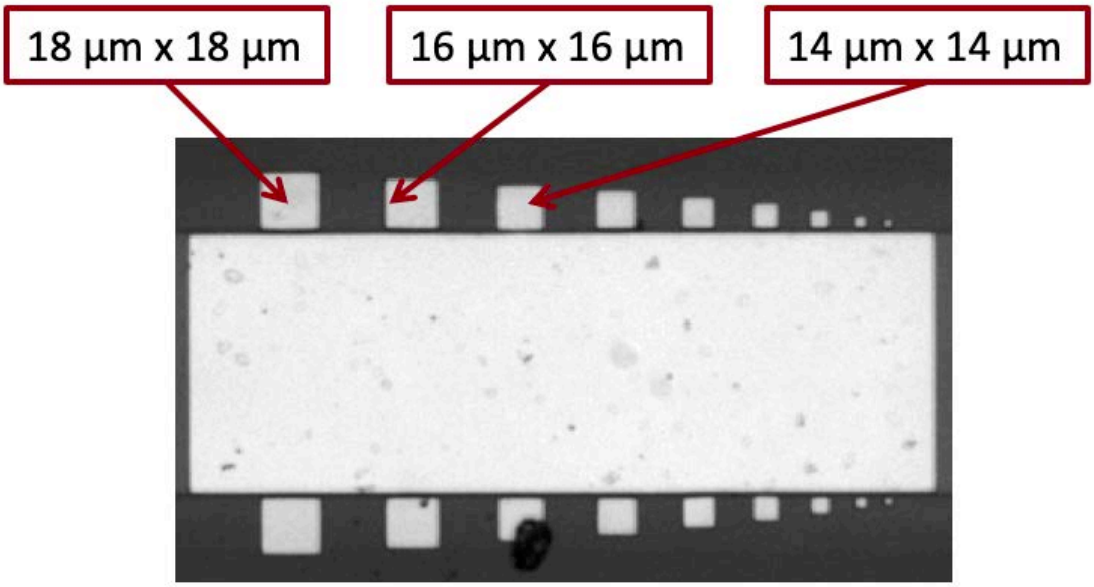

Figure 5.5: Structure of a complete set of devices in a cell with different dimensions an the relative ground pad

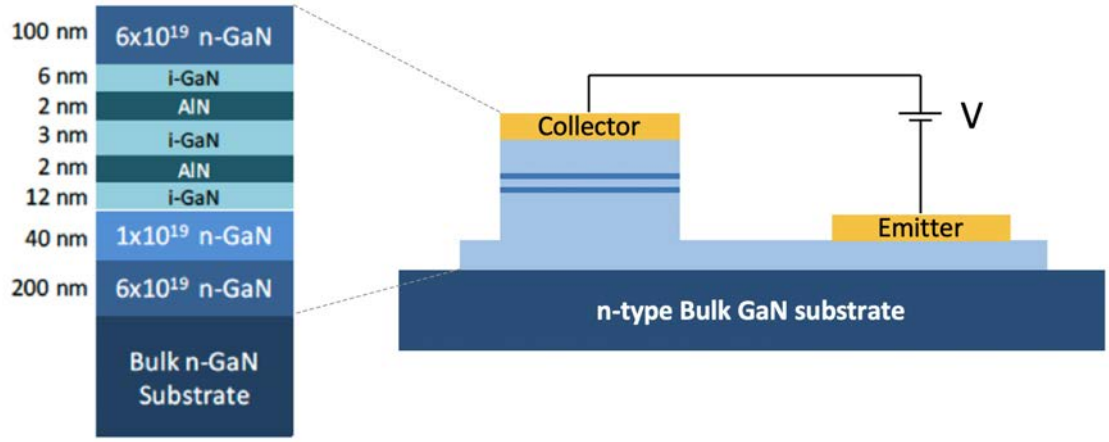

Figure 5.6: Section of the tested devices

to investigate the variability of the fundamental parameters of the RTDs, in the different test structures of the wafer. During the analysis, we increased the forward voltage from $0\,V$ up to $7\,V$, with an integration time of $1\,PLC$ ($20\,ms$).

The resulting I-V curves can be seen in Figure 5.7 and in Figure 5.8.

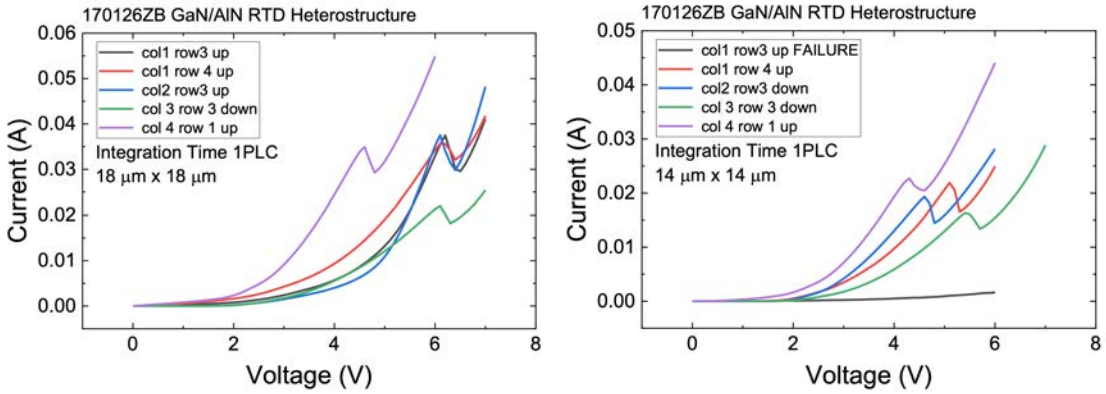

Figure 5.7: Preliminary I-V curves on various devices

The great variability between identical devices in different test structures is immediately clear and is probably related to the variability in the thickness of the super-thin barrier layers. In fact, a single monolayer (ML) fluctuation in barrier thickness can bring substantial variation to the tunneling current [29].

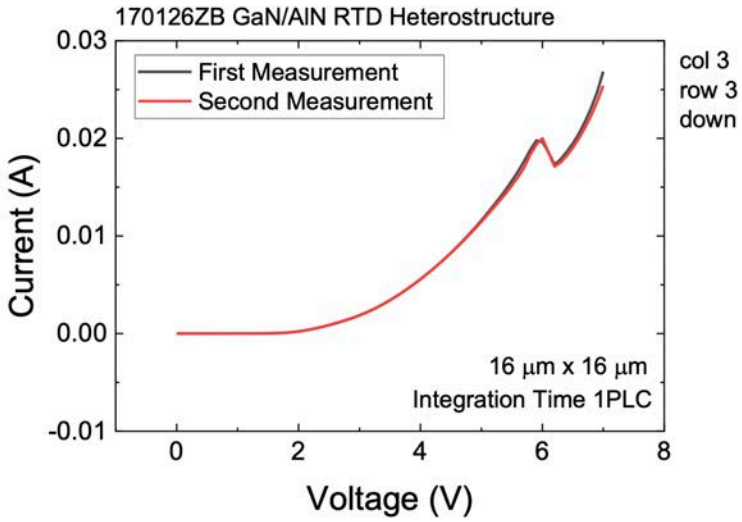

Figure 5.8: I-V measurements repeated twice in a row on the same device

The tested devices showed also good repeatability in case of consecutive measurements, thus demonstrating the absence of degradation due to the measurement setup.

Moreover, we analyzed the dependence of the I-V characteristic on the integration time, by

testing 3 devices with the same dimension ($18\ \mu m$) in different test structures, with a integration time going from $80\ \mu s$ ($1\ MM$ or Manual Mode) up to $2\ s$ (100 power line cycles or PLC).

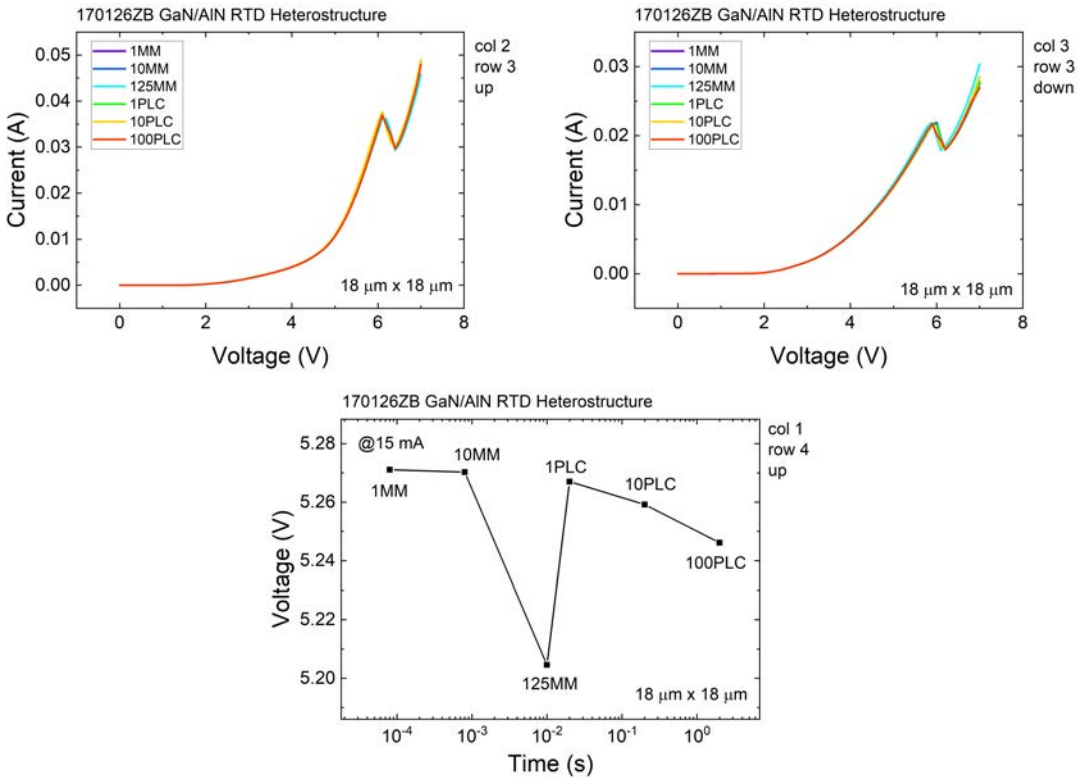

Figure 5.9: I-V measurements performed at different integration times

As can be seen in Figure 5.9, a dependence on the integration time is not visible both at $40\ mA$ and $25\ mA$, so we can say that no trapping phenomena that can potentially affect the reliability are induced, neither for long integration time.

5.3 Temperature dependence of the I-V characteristic

After the preliminary characterization, to better understand which phenomena lead to the presence of the NDC, we analyzed the temperature dependence of the I-V characteristic of our resonant tunneling diodes. Therefore, we tested 2 different devices with the same dimension ($18\ \mu m$) on different test structures, at temperatures going from $30\ ^\circ C$ up to $130\ ^\circ C$.

As we can see in Figure 5.10, the valley voltage, the peak voltage and current are independent from temperature because they are originated from the resonant tunneling phenomena and so they depends only on the alignment of the band diagram. On the other side, for voltages higher than the peak voltage, the current increases with increasing temperatures, due to the increase of the scattering processes.

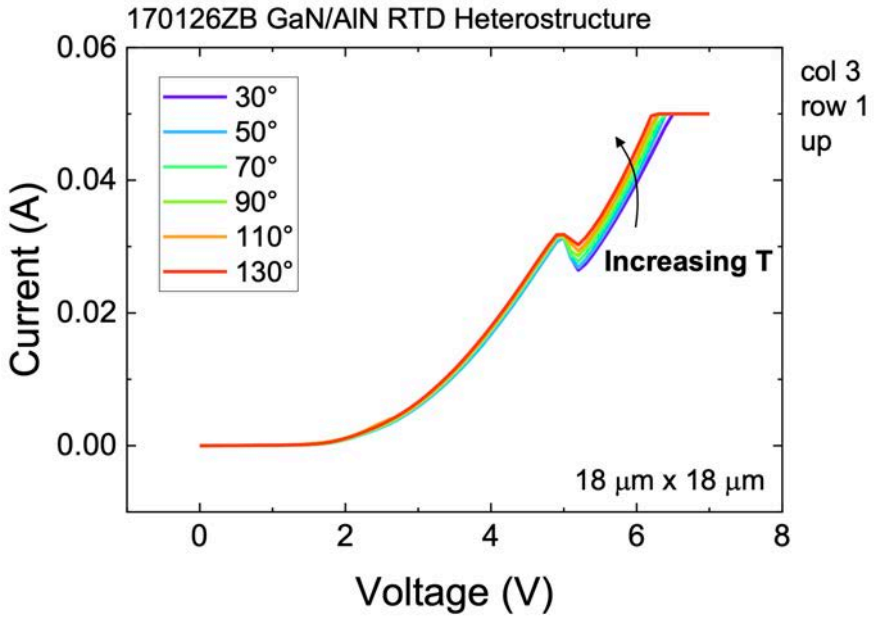

Figure 5.10: I-V performed at different temperatures

It is also important to note a slight shift upwards of the entire I-V characteristic which is linked to the enhancement of thermionic and other thermally activated transport mechanisms at higher temperatures [30].

As can be seen in Figure 5.11, the width of the NDC region does not change with respect to temperature, but the valley current does, so we have a change in the slope of the I-V characteristic related to the increasing temperature in the NDC region. In particular, for higher temperatures, we have smaller negative conductance.

In Figure 5.12 it is possible to see how various parameters of the I-V characteristic change with respect to temperature.

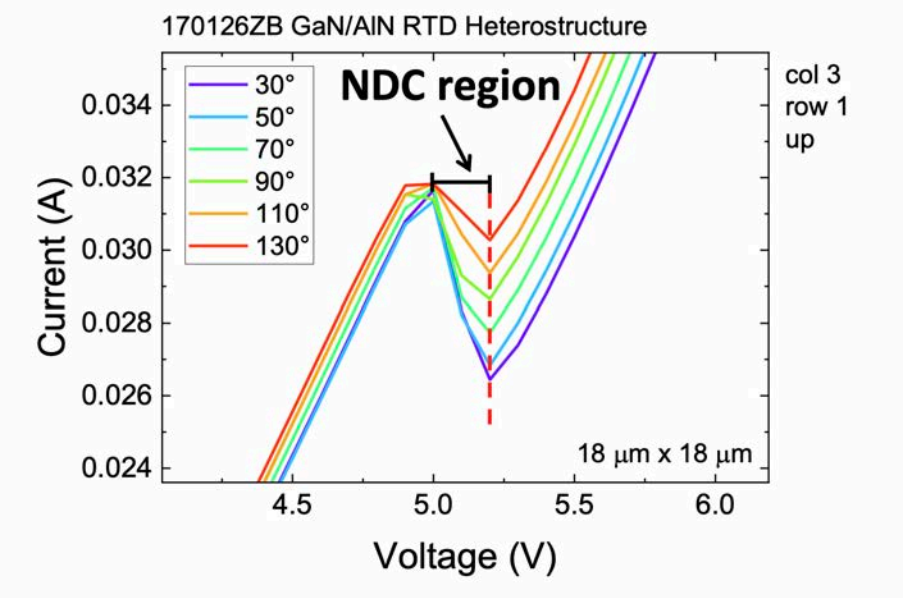

Figure 5.11: Zoom of the I-V curves obtained at different temperatures

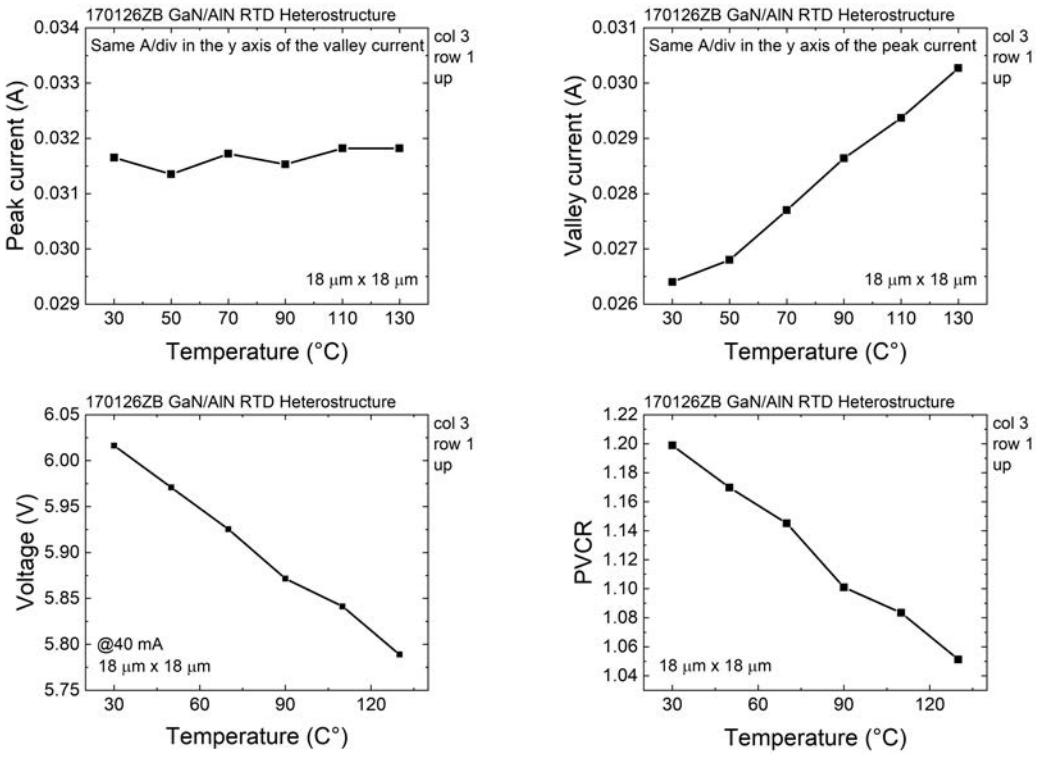

Figure 5.12: Various parameters extracted from the I-V curve in respect to the temperature

As expected from theoretical predictions for double-barrier heterostructure based RTDs [31], the PVCR (Peak to Valley Current Ratio) decreases with increasing temperature. This decrease in PVCR is related to the broadening of the supply function that enhances the non-resonant component of tunneling current [30]. This can cause the valley current to increase a lot more than the peak one and so causing the shrinking of the PVCR.

The temperature dependence of the PVCR was also the cause of the initial appearance of the NDC only at extremely low temperatures: in fact, in early devices, the NDC was not visible at room temperature due to the predominance of thermally activated transport methods [32].

6

Conclusions

This thesis work deals with the study of two types of vertical diodes based on bulk gallium nitride, both provided by Cornell University.

The first set of devices is composed by two generations of polarization-doped diodes with the main difference being the higher carbon concentration in devices of the first generation. For these devices we carried out optical and electrical characterizations in order to study trapping phenomena and the impact of different carbon concentration on GaN-based devices. In particular, in order to characterize the presence of deep levels in the devices, we performed capacitance deep levels transient spectroscopy (C-DLTS) measurements at different voltage and temperatures. This analysis allowed us to obtain an Arrhenius plot confirming the presence of carbon on nitrogen sites in these devices.

To further investigate the presence of carbon in these devices, we performed deep level optical

spectroscopy (DLOS) measurements. From this analysis we obtained the steady state photocapacitance (SSPC) spectrum, and by analyzing the change in the slope of this spectrum we indentified the energy of an emission process, characterizing it at different bias conditions. The obtained energies are consistent with previously obtained values for substitutional carbon defects. Moreover, the emission energy showed a decreasing trend as the applied reverse voltage increased; consistent with the Poole-Frenkel effect. This effect consist of an enhancement of the emission rate due to the bending of the energy bands in presence of a strong electric field. An electro-optical characterization at different temperatures was also carried out. In particular we acquired I-V characteristics and emission spectra of both generations at temperatures from $80\ K$ to $350\ K$. We compared the I-V curves and spectra of the polarization-doped diodes also with an impurity-doped vertical GaN-on-GaN diode. From this comparison we were able to see a hump only present in the first generation of polarization-doped diodes and in the impurity-doped diodes. This phenomenon could be related to a different compensation of the n-type doping due to the higher carbon concentration of these two samples. From the spectra we were able to recognize some photoluminescence bands typical of GaN such as the blue luminescence band (BL), the yellow luminescence band (YL) and two peaks located in the UV luminescence band. From the analysis of these peaks we were able to confirm the important roles that carbon and magnesium have on the behaviors of these devices.

The second set of devices is composed of resonant tunneling diodes (RTDs) based on a GaN/AlGaN double-heterostructure. To better understand the role of defects in the resonant tunneling phenomena we carried out an I-V characterization under different temperature conditions. From these measurements we were able to observe that the peak-to-valley current ratio (PVCR) decreases with increasing temperature due to the enhancement of the non-resonant component of tunneling current. This temperature dependence of the PVCR was also the cause of the initial problems in achieving room-temperature resonant tunneling in nitride-based RTDs.

The results reported above have provided useful information about the influence of defect

on vertical GaN devices. In particular, the results obtained on these diodes can contribute to the understanding of the physical mechanisms which can take place in more complex devices. Therefore, these results are very important for the future development of efficient and reliable vertical devices, which will be a key element for the electronic devices of the future.

List of Figures

Bibliography

[1] J. Millán and P. Godignon, "Wide band gap power semiconductor devices," in *2013 Spanish Conference on Electron Devices*, Feb 2013, pp. 293–296.

[2] R. Izumi, S. Suzuki, and M. Asada, "1.98 thz resonant-tunneling-diode oscillator with reduced conduction loss by thick antenna electrode," in *2017 42nd International Conference on Infrared, Millimeter, and Terahertz Waves (IRMMW-THz)*. IEEE, 2017, pp. 1–2.

[3] M. Meneghini, G. Meneghesso, and E. Zanoni, *Power GaN Devices: Materials, Applications and Reliability*, 01 2017.

[4] T. Paskova and K. R. Evans, "Gan substrates—progress, status, and prospects," *IEEE Journal of Selected Topics in Quantum Electronics*, vol. 15, no. 4, pp. 1041–1052, July 2009.

[5] C. G. Van de Walle, "Defects and doping in gan," *equilibrium*, vol. 5, no. 14, p. 15.

[6] S. Li, T. Zhang, J. Wu, Y. Yang, Z. Wang, Z. Wu, Z. Chen, and Y. Jiang, "Polarization induced hole doping in graded al x ga1- x n (x= 0.7 1) layer grown by molecular beam epitaxy," *Applied Physics Letters*, vol. 102, no. 6, p. 062108, 2013.

[7] Y. . Wu, A. Saxler, M. Moore, R. P. Smith, S. Sheppard, P. M. Chavarkar, T. Wisleder, U. K. Mishra, and P. Parikh, "30-w/mm gan hemts by field plate optimization," *IEEE Electron Device Letters*, vol. 25, no. 3, pp. 117–119, March 2004.

[8] I. C. Kizilyalli, A. P. Edwards, H. Nie, D. Bour, T. Prunty, and D. Disney, "3.7 kv vertical gan pn diodes," *IEEE Electron Device Letters*, vol. 35, no. 2, pp. 247–249, Feb 2014.

[9] I. C. Kizilyalli, A. Edwards, D. Bour, H. Shah, H. Nie, and D. Disney, "Vertical devices in bulk gan drive diode performance to near-theoretical limits," *How2Power Today*, 2013.

[10] C. Seager, A. Wright, J. Yu, and W. Götz, "Role of carbon in gan," *Journal of applied physics*, vol. 92, no. 11, pp. 6553–6560, 2002.

[11] J. Neugebauer and C. G. Van de Walle, "Gallium vacancies and the yellow luminescence in gan," *Applied Physics Letters*, vol. 69, no. 4, pp. 503–505, 1996.

[12] J. Lyons, A. Janotti, and C. Van de Walle, "Carbon impurities and the yellow luminescence in gan," *Applied Physics Letters*, vol. 97, no. 15, p. 152108, 2010.

[13] J. Lyons, A. Janotti, and V. de Walle, "Effects of carbon on the electrical and optical properties of inn, gan, and aln," *Physical Review B*, vol. 89, no. 3, p. 035204, 2014.

[14] O. Mitrofanov and M. Manfra, "Poole-frenkel electron emission from the traps in algan/gan transistors," *Journal of Applied Physics*, vol. 95, no. 11, pp. 6414–6419, 2004.

[15] J. Simon, V. Protasenko, C. Lian, H. Xing, and D. Jena, "Polarization-induced hole doping in wide–band-gap uniaxial semiconductor heterostructures," *Science*, vol. 327, no. 5961, pp. 60–64, 2010.

[16] E. Fabris, C. De Santi, A. Caria, K. Nomoto, Z. Hu, W. Li, X. Gao, D. Jena, H. G. Xing, G. Meneghesso *et al.*, "Breakdown walkout in polarization-doped vertical gan diodes," *IEEE Transactions on Electron Devices*, vol. 66, no. 11, pp. 4597–4603, 2019.

[17] D. Lang, "Deep-level transient spectroscopy: A new method to characterize traps in semiconductors," *Journal of applied physics*, vol. 45, no. 7, pp. 3023–3032, 1974.

[18] M. Caesar, M. Dammann, V. Polyakov, P. Waltereit, W. Bronner, M. Baeumler, R. Quay, M. Mikulla, and O. Ambacher, "Generation of traps in algan/gan hemts during rf-and dc-stress test," in *2012 IEEE International Reliability Physics Symposium (IRPS)*. IEEE, 2012, pp. CD–6.

[19] M. Meneghini, C. de Santi, T. Ueda, T. Tanaka, D. Ueda, E. Zanoni, and G. Meneghesso, "Time-and field-dependent trapping in gan-based enhancement-mode transistors with p-gate," *IEEE Electron device letters*, vol. 33, no. 3, pp. 375–377, 2012.

[20] J. Osaka, Y. Ohno, S. Kishimoto, K. Maezawa, and T. Mizutani, "Deep levels in n-type algan grown by hydride vapor-phase epitaxy on sapphire characterized by deep-level transient spectroscopy," *Applied Physics Letters*, vol. 87, no. 22, p. 222112, 2005.

[21] K. Tanaka, M. Ishida, T. Ueda, and T. Tanaka, "Effects of deep trapping states at high temperatures on transient performance of algan/gan heterostructure field-effect transistors," *Japanese Journal of Applied Physics*, vol. 52, no. 4S, p. 04CF07, 2013.

[22] M. A. Reshchikov and H. Morkoç, "Luminescence properties of defects in gan," *Journal of applied physics*, vol. 97, no. 6, pp. 5–19, 2005.

[23] R. Armitage, W. Hong, Q. Yang, H. Feick, J. Gebauer, E. Weber, S. Hautakangas, and K. Saarinen, "Contributions from gallium vacancies and carbon-related defects to the "yellow luminescence" in gan," *Applied physics letters*, vol. 82, no. 20, pp. 3457–3459, 2003.

[24] W. Götz, N. Johnson, J. Walker, D. Bour, and R. Street, "Activation of acceptors in mg-doped gan grown by metalorganic chemical vapor deposition," *Applied Physics Letters*, vol. 68, no. 5, pp. 667–669, 1996.

[25] J. Söderström and T. G. Andersson, "Gaasalgaas resonant tunneling diodes: The dependence of the peak-to-valley current ratio on barrier thickness and height," *Superlattices and Microstructures*, vol. 5, no. 1, pp. 109–113, 1989.

[26] T. A. Growden, D. F. Storm, W. Zhang, E. R. Brown, D. J. Meyer, P. Fakhimi, and P. R. Berger, "Highly repeatable room temperature negative differential resistance in aln/gan resonant tunneling diodes grown by molecular beam epitaxy," *Applied Physics Letters*, vol. 109, no. 8, p. 083504, 2016.

[27] B. Gil, *III-Nitride Semiconductors and their modern devices*. OUP Oxford, 2013, vol. 18.

[28] J. Encomendero, F. A. Faria, S. Islam, V. Protasenko, S. Rouvimov, B. Sensale-Rodriguez, P. Fay, D. Jena, and H. G. Xing, "New tunneling features in polar iii-nitride resonant tunneling diodes," *Physical Review X*, vol. 7, no. 4, p. 041017, 2017.

[29] J. Encomendero, R. Yan, A. Verma, S. Islam, V. Protasenko, S. Rouvimov, P. Fay, D. Jena, and H. G. Xing, "Room temperature microwave oscillations in gan/aln resonant tunneling diodes with peak current densities up to 220 ka/cm2," *Applied Physics Letters*, vol. 112, no. 10, p. 103101, 2018.

[30] D. Li, J. Shao, L. Tang, C. Edmunds, G. Gardner, M. Manfra, and O. Malis, "Temperature-dependence of negative differential resistance in gan/algan resonant tunneling structures," *Semiconductor Science and Technology*, vol. 28, no. 7, p. 074024, 2013.

[31] J. Chen, J. Chen, C. Yang, and R. Wilson, "The i-v characteristics of double-barrier resonant tunneling diodes: Observation and calculation on their temperature dependence and asymmetry," *Journal of applied physics*, vol. 70, no. 6, pp. 3131–3136, 1991.

[32] U. Gennser, V. Kesan, S. Iyer, T. Bucelot, and E. Yang, "Temperature dependent transport measurements on strained si/si1- x ge x resonant tunneling devices," *Journal of Vacuum Science & Technology B: Microelectronics and Nanometer Structures Processing, Measurement, and Phenomena*, vol. 9, no. 4, pp. 2059–2063, 1991.

Ringraziamenti

Un sentito ringraziamento va al professor Meneghini ed al gruppo di microelettronica per avermi permesso di svolgere questa attività di tesi. Un ringraziamento particolare ad Elena per la disponibilità e la gentilezza con cui mi ha seguito e consigliato.

Ringrazio tutti gli amici che hanno deciso di starmi vicino durante questi anni e che, anche se in piccola parte, hanno contribuito alla riuscita di questa impresa. Grazie ai non integrati che pur essendo lontani, sono sempre i più vicini.

Ringrazio in maniera particolare Francesca, Fabiana, Raffaele e Gianfabio per aver reso la mia permanenza in "Casa Curiel" una delle esperienze più belle della mia vita. Grazie per le pizze kebab, per le cavolate insieme e per i sorrisi che siete sempre riusciti a strapparmi appena varcato l'uscio di quella che ho veramente vissuto come casa mia.

Ringrazio mia sorella Giulia per le nostre chiacchierate, per il sostegno che mi ha sempre dato e per il fantastico rapporto che abbiamo e spero avremo sempre.

Ringrazio mia madre per essermi stata affianco in ogni momento, ricordandosi di chiamarmi anche, e soprattutto, quando me ne dimenticavo io. Per essersi presa cura di me da sempre e per avermi trattato nel miglior modo che io potessi mai desiderare.

Ringrazio mio padre per avermi supportato, aiutato ma soprattutto per avermi sgridato quando era necessario. Sei probabilmente la migliore persona che io conosca e non posso che essere fiero di averti con me.

A Silvia, la mia metà, dedico con amore questo intero lavoro, con la speranza che non sia la fine di qualcosa ma che sia solamente il primo passo della nostra lunga vita insieme.